Hindawi
Advances in Civil Engineering
Volume 2024, Article ID 7258680, 40 pages
https://doi.org/10.1155/2024/7258680

Research Article

Dynamic Properties and Dynamic Response Model of Jointed Granites by Cyclic Loading

Xiaobin Ding,[1,2] **Junxing Zhao**,[1] **and Yaojun Dong**[1]

[1]*School of Civil Engineering and Transportation, South China University of Technology, Guangzhou 510641, Guangdong, China*
[2]*Guangdong Provincial Key Laboratory of Modern Civil Engineering Technology, South China Institute of Geotechnical Engineering, Guangzhou, Guangdong, China*

Correspondence should be addressed to Junxing Zhao; 410162057@qq.com

Received 18 September 2023; Revised 24 November 2023; Accepted 26 December 2023; Published 7 February 2024

Academic Editor: Hai-Tao Zhu

The present study investigates the dynamic properties of granite samples with varying degrees of defects through triaxial cyclic loading experiments conducted under different conditions, including varied confining pressures, loading frequencies, dynamic stress amplitudes, and number of cycles, and the dynamic response model of granite samples influenced by the confining pressure and frequency are constructed. The results show that the dynamic elastic modulus of granite increases, but its dynamic damping ratio decreases as the confining pressure increases. The dynamic elastic modulus and dynamic damping ratio of the granite increase as increasing frequency. The dynamic elastic modulus of granite increases with the increasing dynamic stress amplitude while its dynamic damping ratio decreases. The dynamic elastic modulus and dynamic damping ratio of granite decreases with an increasing number of cycles. The modified Duncan–Chang model can well describe the dynamical behavior of granite influenced by the confining pressure and frequency. The correlation coefficients of the modified model reached 0.98. It is worth saying that the correlation coefficient of the model is low at 20 Hz frequency. It indicates that frequency has a strong effect on the dynamic response of granite compared with the confining pressure. These data and models will be applied to the next step of detection and prediction of the tunnel rock stress state.

1. Introduction

In nature, tunnel rocks experience diverse pressure conditions, yet they maintain a state of stable equilibrium under these various pressure constraints. However, the presence of gravity, potential rock-soil sliding, hollow spaces within the rock, groundwater concentration, or rock mass movement (as depicted in Figure 1) can lead to stress concentration within the tunnel rock. This concentration may disturb the original stress equilibrium of the tunnel rock, potentially resulting in hazardous incidents. Consequently, obtaining accurate information about the stress state of the tunnel rock is crucial to prevent accidents and ensure safety.

Many researchers have found that the stress state of rocks is related to the wave velocity. Aghaei et al. [1] found that changes in wave velocities are dependent on a range of petrophysical parameters, elastic modulus, and stress conditions. Jin et al. [2] found that the application of different stresses has an effect on the rock stress wave velocity and affects the attenuation law of the stress waves. Jia et al. [3] conducted uniaxial compression tests on the rocks and found a correlation between the wave velocity and the current stress state of the rocks. The conclusions of these researchers indicate that if we have difficulties to measure the rock stress state, detecting the wave velocity changes is a feasible approach [4, 5].

In summary, we propose a method to detect the working state of the tunnel rock by using shock waves. The workflow is shown in Figure 2. The shock wave transmitting and receiving devices are mounted on a robotic arm. During the detection process, the shock wave transmitting device emits shock waves toward the target rock. The resulting mechanical vibration waves propagate within the target rock and are subsequently captured by the collection device, allowing for the acquisition of the mechanical attenuation characteristics of the target rock. Then, the mechanical wave is compared with the original waveform to get the current

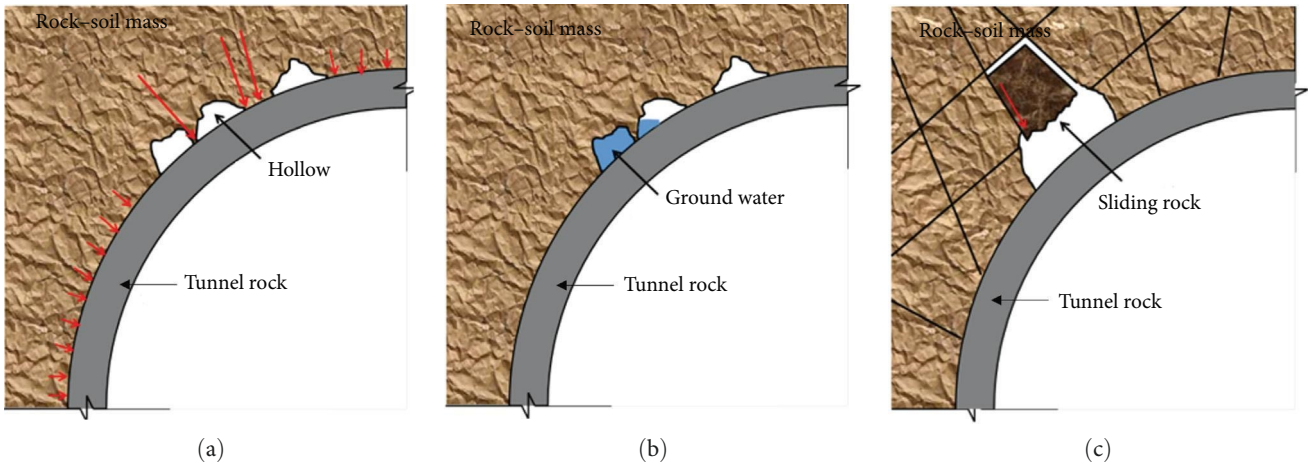

FIGURE 1: Stress change situation: (a) hollow, (b) groundwater, and (c) sliding rock.

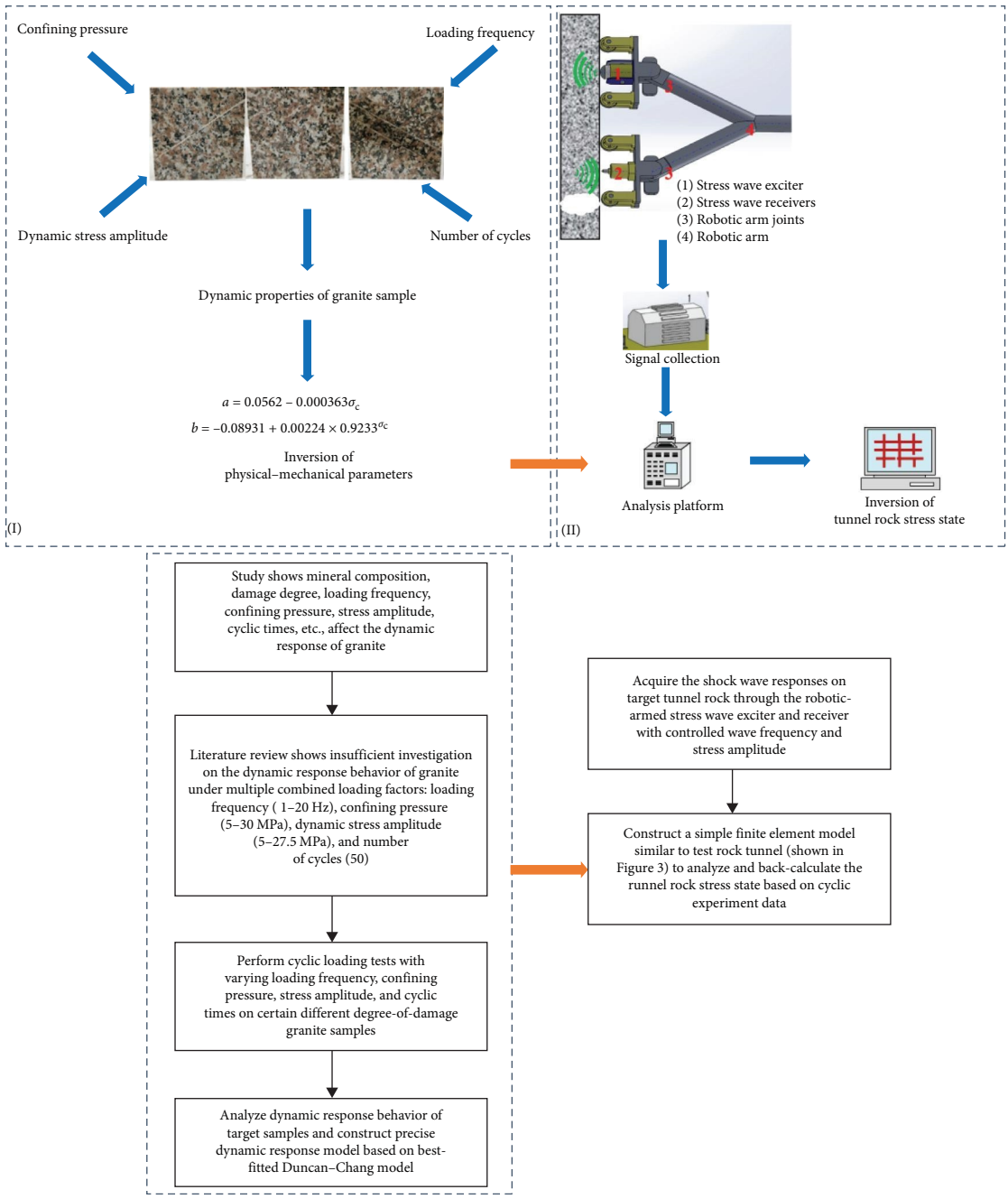

FIGURE 2: Workflow.

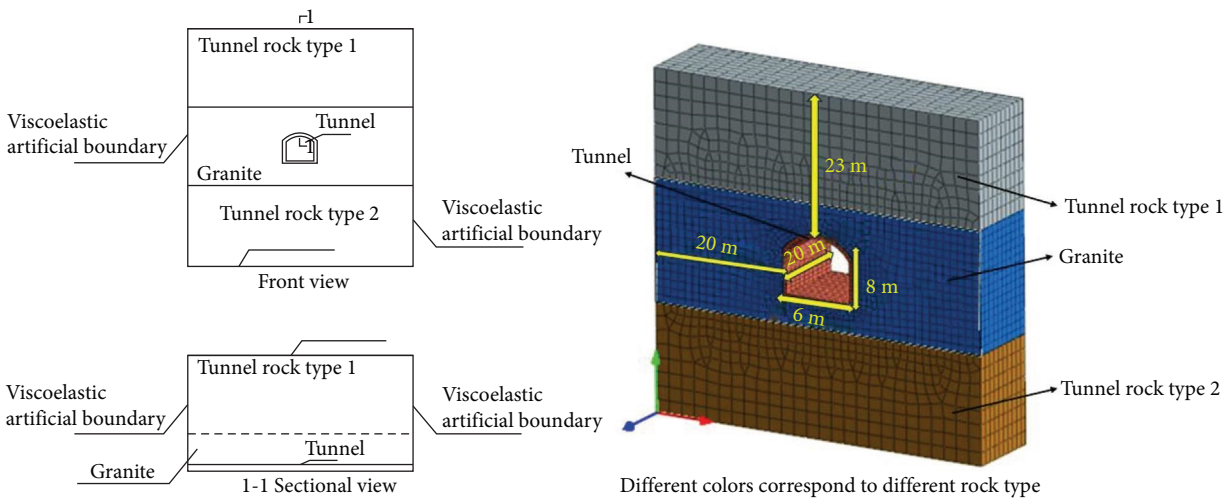

Figure 3: Schematic of target detection tunnel.

working state of the targe rock. According to previous studies, the rock will show different dynamic response characteristics under different influence conditions. If we know the dynamic response model of the rock under the influence of such confining pressure and frequency, then we can use this model to predict the working state of the target rock under specific conditions.

Once the dynamic response behavior has been thoroughly analyzed and an accurate constitutive model has been established, a simplified numerical representation is formulated based on the structural characteristics of the test tunnel wall. The iterative solution process is then applied iteratively, ensuring that stress solutions align consistently for the rock wall under varying loading frequencies and amplitudes. A visual representation of the target tunnel configuration is depicted in Figure 3. The tunnel under examination possesses dimensions of 6 m in width, 8 m in height and is buried at a depth of 23 m. The numerical model's boundary is set at a distance of 20 m from the tunnel limit. The tunnel excavation spans a length of 20 m, and the tunnel structure adheres to a straight-wall arch tunnel lining design.

We divided the study into two parts according to the progress of work completion. The research is as follows: (I) Obtain the variables affecting the dynamic properties of the rock samples through literature research. The experiments were carried out after confirming the test variables based on the conditions available in the laboratory. The dynamic properties of rock samples are obtained by controlling the variables to perform cyclic loading tests on the rock samples. Then, the dynamic response model of the rock sample is constructed, and the material parameter formulas are obtained. (II) Using shock waves to collect information on the target rock, such as wave velocity and frequency. Using the materials parameter formulas obtained in Part (I), the primary stress can be deduced by combining the iterative correction of the internal stress field of the target rock. Therefore, the key to the success of our work is to obtain the dynamic properties of the targe rock under different influences and its dynamic response model.

2. Literature Review and Discussion

Many scholars have investigated the rock dynamic properties by controlling different variables. Bagde et al. [6] conducted cyclic loading tests with sandstone at different loading frequencies and amplitudes and found the dynamic fatigue strength and the dynamic axial stiffness of the rock reduced with loading frequencies and amplitude. The dynamic modulus increases with the loading frequency but decreases with the amplitude. Ma et al. [7] found that the elastic modulus of rock salt under cyclic loading increases with increasing confining pressure and decreases with increasing loading cycles. Li et al. [8] found that the dynamic strength of gypsum samples with man-made intermittent joints decreases with loading cycles, and the deformation modulus increases with the dynamic loading frequency. Liu et al. [9] found that dip angle, persistence, density, and spacing have significant effects on the fatigue properties of rocks, and the variation pattern of elastic energy was found. Ma et al. [10] found that the elastic modulus of yellow sandstone increased with the increase of maximum cyclic stress by cyclic loading test. Deng et al. [11] found that the damping ratio of sandstone under cyclic loading increases with increasing frequency and decreases with increasing stress amplitude. The dynamic elastic modulus increases with increasing stress amplitude and frequency. Ni et al. [12] conducted cyclic loading tests on granite and found that the granite hysteretic loop area, dynamic elastic modulus, and damping ratio increased with frequency increasing. Huang et al. [13] found that at the same strain, the dynamic elastic modulus of red clay increases with the increase of surrounding pressure and decreases with the increase of loading frequency. The damping ratio decreases with the increase of the surrounding pressure. Bieand and Liu [14] obtained from the test that the dynamic elastic modulus and dynamic damping ratio of phyllite decrease with increasing stress amplitude. Yang et al. [15] conducted tests and obtained results showing that the peak strength and elastic modulus decreased with increasing temperature. Zhao et al. [16] found that the elastic modulus

and Poisson's ratio decrease with increasing initial confining pressures. Xie et al. [17] found that the dynamic compressive strength of both unjointed intact and jointed rock specimens increased with the increase of loading rate and confining pressure, and with the increase of loading rate, jointed rock specimens exhibited more obvious plastic deformation capacity than intact rock specimens

Table 1 summarizes the variables controlled by different researchers studying the dynamic properties of rocks. By researching the literature, we found that the experiments designed by researchers are sufficiently complete, and a large number of research results have been obtained. Based on the aim desired for this test, we felt that some improvements could be made to facilitate the use of the test results to detect the current working state of the target rock in Part (II). For example, most scholars have controlled for variables of one, two, or three, which is not enough for the purpose of our present experiment. Also, the constrained range of controlled variables in this study restricted the ability to draw extensive conclusions regarding the dynamic properties of granite under the combined influence of multiple factors. Further research incorporating a broader range of controlled variables would be necessary to achieve a more comprehensive understanding of the dynamic behavior of granite specimens. Therefore, we added more test variables and expanded the range of test variables in an experiment to allow us to perform better back analysis of the target rock working states. Therefore, considering the laboratory conditions available, we set the experimental variables as loading frequency (1–20 Hz), confining pressure (5–30 MPa), dynamic stress amplitude (5–27.5 MPa), number of cycles (50 times), and degree of sample defects (single jointed 30°, single jointed 60°, and double jointed 60°).

Tests on intact rocks ($D = 0$), we have completed and obtained the corresponding data [34]. In this paper, we perform cyclic loading tests on granite samples to obtain the effects of confining pressure, loading frequency, dynamic stress amplitude, number of cycles, and the defect degree on the granite samples. The data and models obtained from the tests will be used for inverse analysis of the working states of the target rocks.

3. Experimental Setup

3.1. Samples Preparation. The granite samples were obtained from Wulian County, Rizhao City, Shandong Province, China (Figure 4). The rocks were made into cubic samples near 102 mm × 102 mm × 102 mm.

We cut the samples according to the preset number of joints and the angle of joints and bonded them by epoxy resin. We finally obtained single jointed 30°, double jointed 30° and single jointed 60° samples and polished them into 100 mm × 100 mm × 100 mm cubic samples. The samples are shown in Figure 5.

After the samples were made, we performed the setting of the test variables. Based on the engineering background, the confining pressure in tests was preset as 5, 10, 20, and 30 MPa, respectively. We wanted to obtain more conclusions of the samples at higher frequencies in the test, so we expanded the frequencies set in the study of Liu et al. [35] to 1–20 Hz. Based on the maximum pressure that the test machine could provide, the maximum dynamic stress amplitude that the sample is subjected to before damage, and the accuracy of the data collected by the machine at high frequencies, the dynamic stress amplitude in tests was preset as 5, 10, 15, 20, 25, and 27.5 MPa. Based on the maximum number of cycles reached before the sample was damaged, the number of cycles in tests was preset as 50 times.

After setting the test variables, we named the samples according to the test variables and the defect degree of samples. One sample from each of the different loading conditions was tested, i.e., seven specimens for each different defect degree of rock. The sample naming and loading conditions are summarized in Table 2. In Table 2, the name "D_{30}5-10" means a single jointed 30° sample tested at a frequency of 5 Hz and confining pressure of 10 MPa. The name "S_{30}5-10" means a double jointed 30° sample tested at a frequency of 5 Hz and confining pressure of 10 MPa. After the naming of the sample was completed, we conducted tests.

3.2. Triaxial Test System. Figure 6 shows a triaxial testing machine used for the test. The machine has a maximum force capacity of 4,000 kN, with a maximum horizontal force capacity of 2,400 kN. Positioned beneath the machine is a vertical dynamic load loading device designed with a maximum power capacity of 400 kN. The force resolution of the loading system in both the vertical and horizontal directions is 0.002 kN, while the displacement resolution is 0.005 mm. The maximum loading speed in the horizontal direction is 400 mm/min. The acquisition device can collect 2,500 data points per second at the time of the test.

The process of loading samples is shown in Figure 7. We divided the loading process into three steps. Step 1: Putting the sample into the loading machine and increasing the pressure in the chamber until it reaches the preset confining pressure of 5, 10, 20, and 30 MPa, and then keep it constant. The loading method is a linear static load. Step 2: In this step, cyclic loading should be ensured to reach 50 number of cycles, and then continue to load the sample until the sample is damaged, and observe the state of sample destruction. We changed the loading frequency and dynamic stress amplitude in the loading process. After all the cycles, we can obtain the data of dynamic stress and dynamic strain.

By loading the samples, we obtain the data of dynamic stress and dynamic strain. Then, the dynamic stress and dynamic strain will be used for the next step to calculate the dynamic elastic modulus and dynamic damping ratio of the sample.

3.3. Test Principle

3.3.1. Defect Degree. We made samples with different numbers and angles of joints with the purpose of trying to quantify the defect degree of the samples. We defined a new variable, D, to quantify the defect degree of the samples, and the quantification formula is as follows:

Table 1: Summary of rock properties study.

References	Rock type	Rock integrity	Loading method	Variables	Parameters
Bagde et al. [6]	Sandstone	Complete	Cyclic loading	Loading frequency (0.1–10 Hz), amplitude (0.05–0.15 mm)	Dynamic modulus, dynamic fatigue strength, dynamic axial stiffness
Ma et al. [7]	Rock salt	Complete	Cyclic loading	Confining pressure (7, 14, 21 MPs), loading cycles (about 800)	Elastic modulus
Li et al. [8]	Gypsum	Incomplete	Cyclic loading	Loading frequency (0.2, 2, 21 Hz), loading cycles (0–20), line of flaw angles (0°−90°)	Dynamic strength, the deformation modulus
Liu et al. [9]	Synthetic rocks	Incomplete	Cyclic uniaxial compression	Relative cycle (0–1.2), line of flaw angles (30°−75°)	Dynamic elastic modulus, dynamic damping ratio
Ma et al. [10]	Sandstone	Incomplete	Cyclic loading	Cyclic stress, cycles, line of flaw angles (0°−60°)	Elastic modulus
Deng et al. [11]	Sandstone	Complete	Cyclic loading	Loading frequency (0.02–1 Hz), stress amplitude (10−35 MPa)	Damping ratio, dynamic elastic modulus
Ni et al. [12]	Granite	Complete	Cyclic loading	Loading frequency (0.01–1 Hz)	Dynamic elastic modulus, damping ratio
Huang et al. [13]	Red clay	Complete	Cyclic loading	Confining pressure (100−200 MPa), loading frequency (1–6 Hz)	Dynamic elastic modulus, damping ratio
Bie et al. [14]	Phyllite	Complete	Triaxial compression	Stress amplitude (10−80 MPa)	Dynamic elastic modulus, dynamic damping ratio
Yang et al. [15]	Granite	Complete	Split Hopkinson pressure bar (SHPB) loading	Temperature (25−900°C)	Peak strength, elastic modulus
Zhao et al. [16]	Sandstone	Complete	Cyclic loading and unloading	Confining pressure (0−50 MPa)	Elastic modulus and Poisson's ratio
Xie et al. [17]	Sandstone	Complete/ incomplete	Split Hopkinson pressure bar (SHPB) loading	Confining pressure (2−10 MPa), line of flaw angles (15°)	Dynamic compressive strength
Xiao et al. [18]	Granite	Complete	Cyclic loading	Number of cycles (0–140), stress amplitude (93.23–100.4 MPa)	Dynamic elastic modulus, dynamic damping ratio
Xu et al. [19]	Granite	Complete	Split Hopkinson pressure bar (SHPB) loading	Strain rates (85.7–143.5 s^{-1}), temperature (25 −150°C)	The dynamic compression strength, dynamic peak stress, elastic modulus
Xiao et al. [20]	Granite	Complete/ incomplete	Split Hopkinson pressure bar (SHPB) loading	Line of flaw angles (0°−90°)	Dynamic strength
Yin et al. [21]	Granite	Complete	Triaxial loading test	Temperature (100−400°C), confining pressure (0−25 MPa)	Peak strength, elastic modulus
Zhao et al. [22]	Granite	Complete	Cyclic loading	Temperature (100−600°C)	Strength, elastic modulus
Huang et al. [23]	Granite	Complete/ incomplete	Cyclic loading	Line of flaw angles (45°), number of flaws (0, 1, 2), temperature (20−900°C)	Peak strength, elastic modulus
Zhao et al. [24]	Granite	Complete	Triaxial loading test	Confining pressure (15−55 MPa)	Elastic modulus
Zhou et al. [25]	Granite	Complete/ incomplete	Thermal–mechanical test	Temperature (25−700°C), ligament angle spans (75°−120°)	Elastic modulus
Wu et al. [26]	Granite	Complete	Split Hopkinson pressure bar (SHPB) loading	Stress wavelengths (0.8–2.0 m), strain rates (20–120 s^{-1})	Dynamic compressive strength
Yin et al. [27]	Granite	Complete	Split Hopkinson pressure bar (SHPB) loading	Temperature (25−300°C), axial pressure (20 MPa)	Uniaxial compressive strength, peak stress, elastic modulus
Li et al. [28]	Granite	Complete/ incomplete	Split Hopkinson pressure bar (SHPB) loading	Impact pressures (0.7–0.9 MPa), joint angle (0°−90°)	Dynamic compressive strength, elastic modulus, transmitted energy ratio, absorbed energy ratio, reflected energy ratio
Liang et al. [29]	Granite	Complete	Split Hopkinson pressure bar (SHPB) loading	Strain rates (19.1–190.5/s)	Ultimate strength, elastic modulus
Mishra et al. [30]	Granite	Complete	Split Hopkinson pressure bar (SHPB) loading	Strain rates (41.31–475.59/s)	Dynamic elastic modulus

Table 1: Continued.

References	Rock type	Rock integrity	Loading method	Variables	Parameters
Guo et al. [31]	Granite	Complete	Split Hopkinson pressure bar (SHPB) loading	Temperature (25−800°C)	Peak stress, peak strain, and elastic modulus
Li et al. [32]	Granite	Complete	Split Hopkinson pressure bar (SHPB) loading	Axial stress (0−70 MPa)	Dynamic strength, dynamic elastic modulus, dynamic strain
Yang et al. [33]	Granite and red sandstone	Complete	Cyclic triaxial compression test	Confining pressures (5–25 MPa)	Dynamic shear modulus, damping ratio
Ding et al. [34]	Granite	Complete	Cyclic loading	Loading frequency (1–20 Hz), confining pressure (5–30 MPa), dynamic stress amplitude (5–27.5 MPa), number of cycles (50 times)	Dynamic elastic module, dynamic damping ratio
This paper	Granite	Incomplete	Cyclic loading	Loading frequency (1–20 Hz), confining pressure (5–30 MPa), dynamic stress amplitude (5–27.5 MPa), number of cycles (50 times), degree of sample defects (single jointed 30°, single jointed 60°, and double jointed 60°)	Dynamic elastic module, dynamic damping ratio

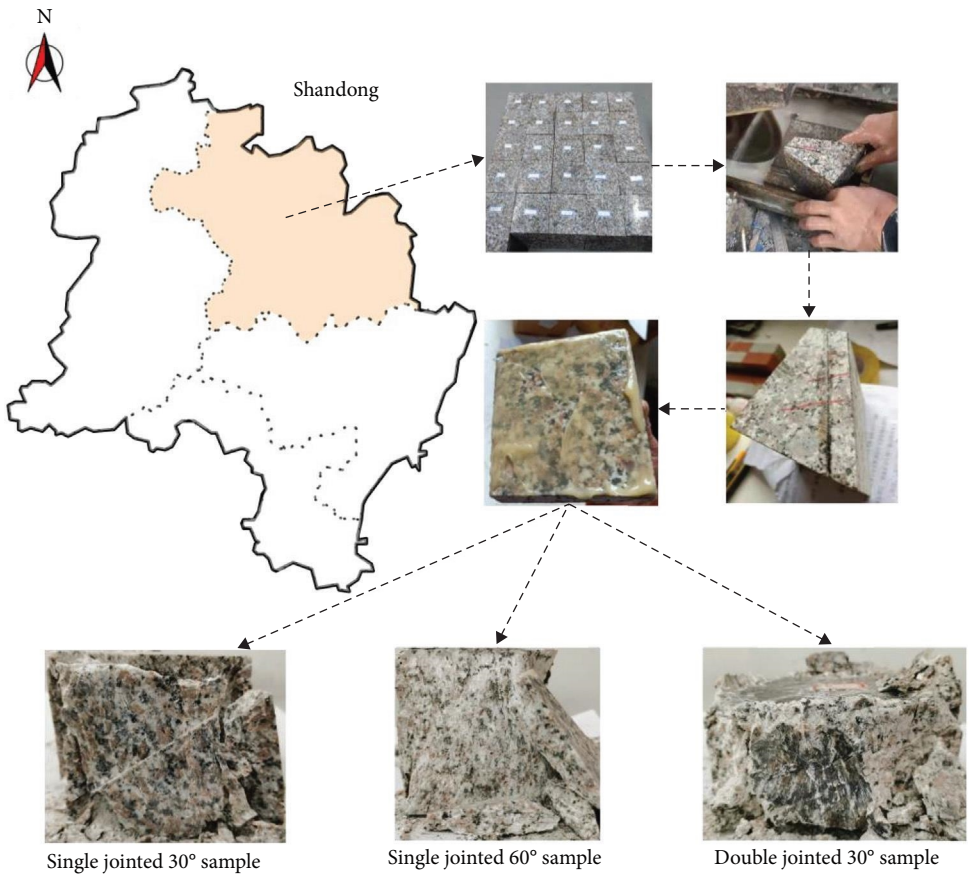

Figure 4: Sample preparation.

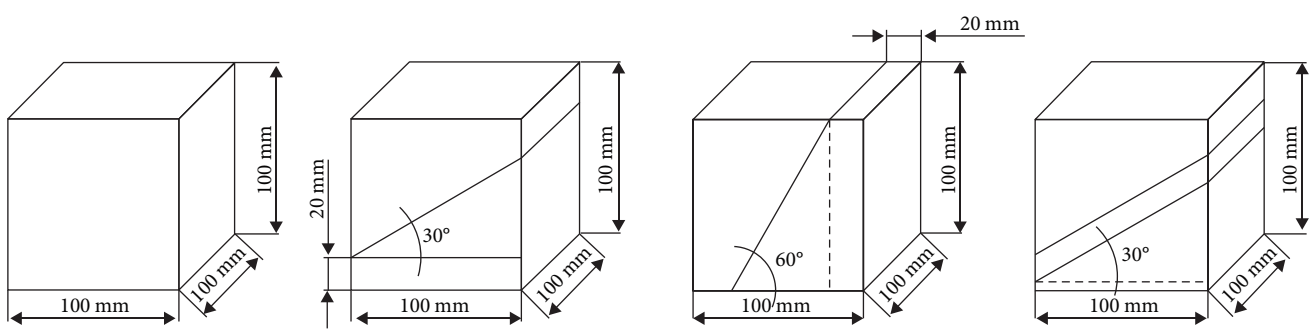

Figure 5: Jointed samples.

$$D = \frac{A_1 + A_2 + \cdots}{S} = \frac{\sum A_i}{S}, \tag{1}$$

where A_i is the area of the surface containing the joint projected on the bottom of the sample, and S is the area of the bottom of the sample.

The samples quantified by the Equation (1) are shown in Figure 8. As shown in Figure 8, the defect degree of samples factors up to 2 and a minimum defect degree factor of 0. The intact sample, i.e., the sample with a defect degree of 0, has already been tested and will not be mentioned again in this test.

3.3.2. Dynamic Elastic Modulus and Dynamic Damping Ratio. The hysteresis loop curves depicting the loading and unloading processes of the samples are presented in Figure 9. The hysteresis loop of the curve represents the energy dissipation during the loading and unloading of the sample. This dissipation can be quantified in terms of the dynamic damping ratio. The dynamic elastic modulus, which is determined as the tangent modulus, characterizes the slope of the stress–strain curve's linear or approximately linear segment. It signifies the sample's elastic modulus when subjected to dynamic loading conditions. The relationship between the dynamic elastic modulus E_d and dynamic damping ratio η is given by Bie and Liu [14] and Deng et al. [11]:

Table 2: Granite samples.

Name	Confining pressure σ_c (MPa)	Frequency f (Hz)	Dynamic stress amplitude $\Delta\sigma_d$ (MPa)	Number of cycles	Rock type
D_{30}5-5	5				
D_{30}5-10	10	5			
D_{30}5-20	20				
D_{30}5-30	30				Single jointed 30° sample
D_{30}1-20		1			
D_{30}10-20	20	10			
D_{30}20-20		20			
D_{60}5-5	5				
D_{60}5-10	10	5			
D_{60}5-20	20				
D_{60}5-30	30		5/10/15/20/25/27.5	50	Single jointed 60° sample
D_{60}1-20		1			
D_{60}10-20	20	10			
D_{60}20-20		20			
S_{30}5-5	5				
S_{30}5-10	10	5			
S_{30}5-20	20				
S_{30}5-30	30				Double jointed 30° sample
S_{30}1-20		1			
S_{30}10-20	20	10			
S_{30}20-20		20			

Figure 6: Triaxial testing machine.

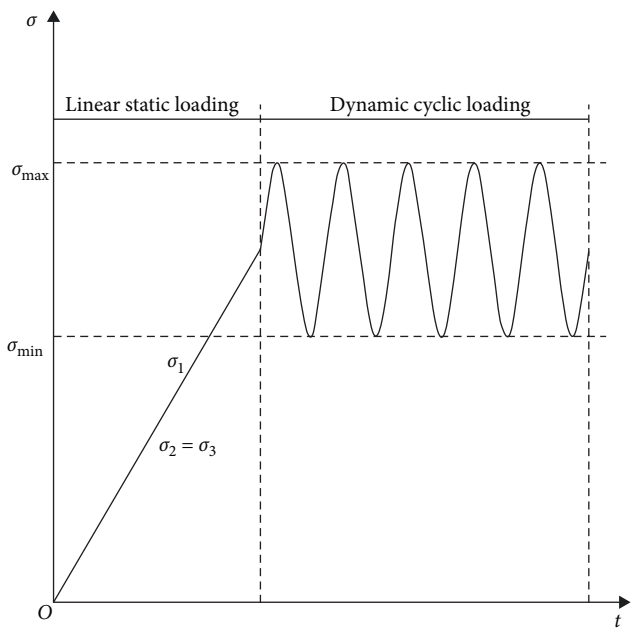

Figure 7: Cyclic loading scheme.

$$E_d = \frac{\sigma_{max} - \sigma_{min}}{\varepsilon_{max} - \varepsilon_{min}}, \quad (2)$$

$$\eta = \frac{1}{4\pi}\frac{S_{ADCBA}}{S_{\Delta OEA}} = \frac{A_R}{4\pi A_S}, \quad (3)$$

where σ_{max} is the maximum dynamic stress. σ_{min} is the minimum dynamic stress. ε_{max} is the maximum dynamic strain. ε_{min} is the minimum dynamic strain. A_R is the area of the hysteresis loop ADCBA and A_S is the area of the triangle OEA.

The dynamic elastic modulus and dynamic damping ratio of the sample, calculated by Equations (1) and (2), we will use in the next step to analyze the results.

4. Results and Discussion

4.1. Hysteresis Loop of Sample

4.1.1. Effect of Confining Pressure. We plot the dynamic stresses and dynamic strains obtained from the tests in Figure 10. Figure 10 shows the hysteresis loop variation for a single jointed 30° sample. According to researchers, the hysteresis loops of rocks under cyclic loading generally show elliptical, crescent-shaped, pointed leaf-shaped, or long eggplant-shaped shapes [36], and it is obvious to see that the hysteresis loop shape of Figure 10 is long eggplant shape. Figure 10 demonstrates that the rock loading curve slope increased with the increase in the confining pressure, and the hysteresis loop area decreased with the increase in the confining pressure. It indicates that the dynamic elastic modulus of granite increased, but the energy loss decreased. Besides, the hysteresis loop area increased with the increase in dynamic stress, indicating that the energy loss of samples increased with the increase in dynamic stress.

4.1.2. Effect of Frequency. Figure 11 shows the hysteresis loop variation for single jointed 30° samples under cyclic loading. Considering the inherent instability of the hysteresis loop curves at high frequencies, the illustration of the samples' hysteresis loop curves at 10–20 Hz emphasizes the relatively stable hysteresis loops. Figure 11 demonstrates that as the frequency increased, the shape of the granite hysteresis loop changed from pointed leaf-shaped to show elliptical. Besides, with the increase in dynamic stress, the granite loading curve slope increased. It indicates the increase in dynamic elastic modulus and energy loss. We can know that the frequency has a large effect on the hysteresis loop of the sample, compared with the confining pressure.

4.1.3. Effect of Defect Degree. Figure 12 shows the variation of the hysteresis loop of the sample at different defect degrees under cyclic loading. Figure 12(a) shows that the hysteresis loop shapes of the samples with different defect degrees are basically the same at the same loading conditions. It indicates that the effect of loading at the same confining pressure and loading frequency on the samples is almost the same. Figure 12(b) shows the variation of the hysteresis loop area of the sample at different number of cycles. The sample hysteresis loop area increases as the defect factor increases.

4.2. Dynamic Properties

4.2.1. Effect of Confining Pressure. Figure 13 shows the variation of the dynamic elastic modulus of the sample with different defect degrees at the confining pressure, dynamic stress amplitude, and number of cycles. The dynamic elastic modulus of samples exhibits distinct patterns in response to these variables. As the number of cycles increases, the dynamic elastic modulus of samples with varying defect degrees experiences a decline, whereas an escalation in the confining pressure or the dynamic stress amplitude correlates with an augmentation in the dynamic elastic modulus. At the confining pressure of 30 MPa and the dynamic stress amplitude of 27.5 MPa, the dynamic elastic modulus of

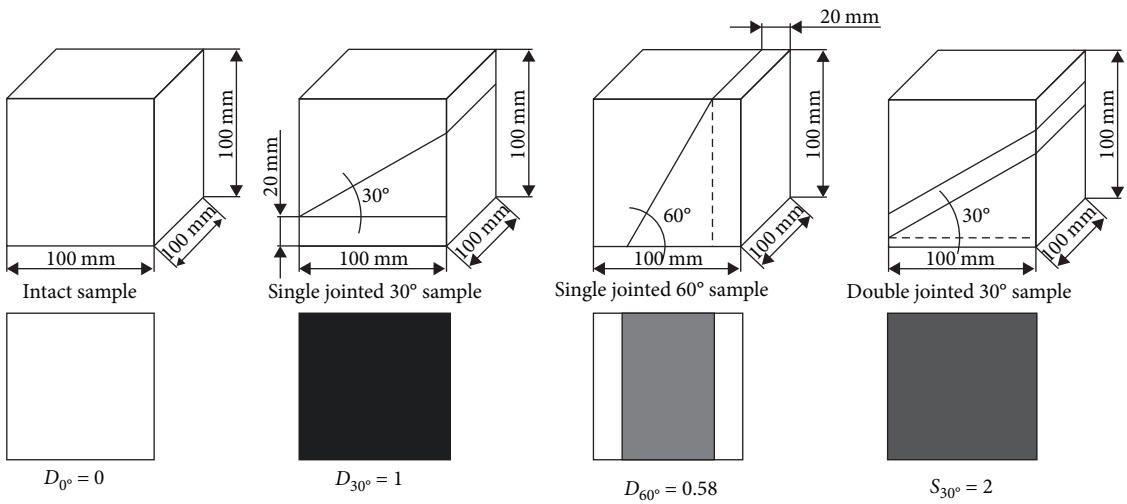

Figure 8: Schematic diagram of the extent of defects in the sample.

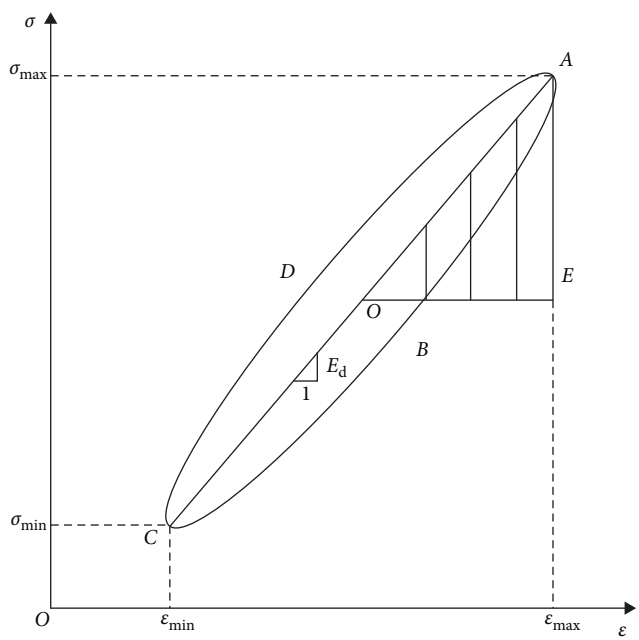

Figure 9: Dynamic stress–strain hysteresis loop.

double jointed 30° sample is significantly smaller than the other samples. It indicates that the dynamic elastic modulus of the samples will be affected at a larger defect degree. Table 3 shows the growth rate of the dynamic elastic modulus of the samples during the increasing confining pressure. We can know that the maximum increases of the samples with different defect degrees are almost the same.

In an endeavor to comprehensively analyze the behavior of the dynamic elastic modulus of samples under varying confining pressures at a constant dynamic stress amplitude, we show the variation of the average dynamic elastic modulus of the samples with black curves in Figure 14. These show that the average dynamic elastic modulus of the samples with different degrees of defects increases with the increasing confining pressure, and the conclusions obtained are consistent with those of Zhang et al. [37] and Chen et al. [38]. It is postulated that the augmentation in confining pressure effectively hampers the development of internal fractures within the granitic material, consequently enhancing the material's capacity to withstand deformation. The trend of the normalized data (normalized with its starting modulus at each line) is shown with blue curves in Figure 14. The blue curves of the single joined 30° samples almost overlap in Figure 14(a), indicating that its dynamic elastic modulus growth rate is almost the same at the dynamic stress amplitude. Figures 14(b) and 14(c) demonstrate that the slope of the blue curve decreases with increasing dynamic stress amplitude, indicating that the growth of the dynamic elastic modulus of the sample decreases with increasing dynamic stress amplitude.

The dynamic damping ratios of the samples with different defect degrees are shown in Figure 15, which are influenced by the number of cycles, the dynamic stress amplitude, and the confining pressure. The dynamic damping ratio of the sample variations is more dramatic in different number of cycles. In general, the dynamic damping ratio of samples with different defect degrees decreases as the number of cycles increases and decreases as the dynamic stress amplitude increases.

Figure 15 shows the variation of the dynamic damping ratio of the sample at the confining pressure, the dynamic stress amplitude, and the number of cycles. The findings indicate a consistent pattern where samples with different defect degrees exhibit a decrease in the dynamic damping ratio as the number of cycles increases, while an increase is observed with an escalation in dynamic stress amplitude. It can be obvious that the dynamic damping ratio of the single jointed 30° sample decreases with the increase of the confining pressure. The conclusion is similar with Zhao et al.'s [39] and Peellage et al.'s [40] results. According to Li et al. [41], increasing the confining pressure can inhibit crack expansion. However, this trend was not obvious in the single jointed 60° sample and the double jointed 30° sample. We postulate that insufficient close contact between internal

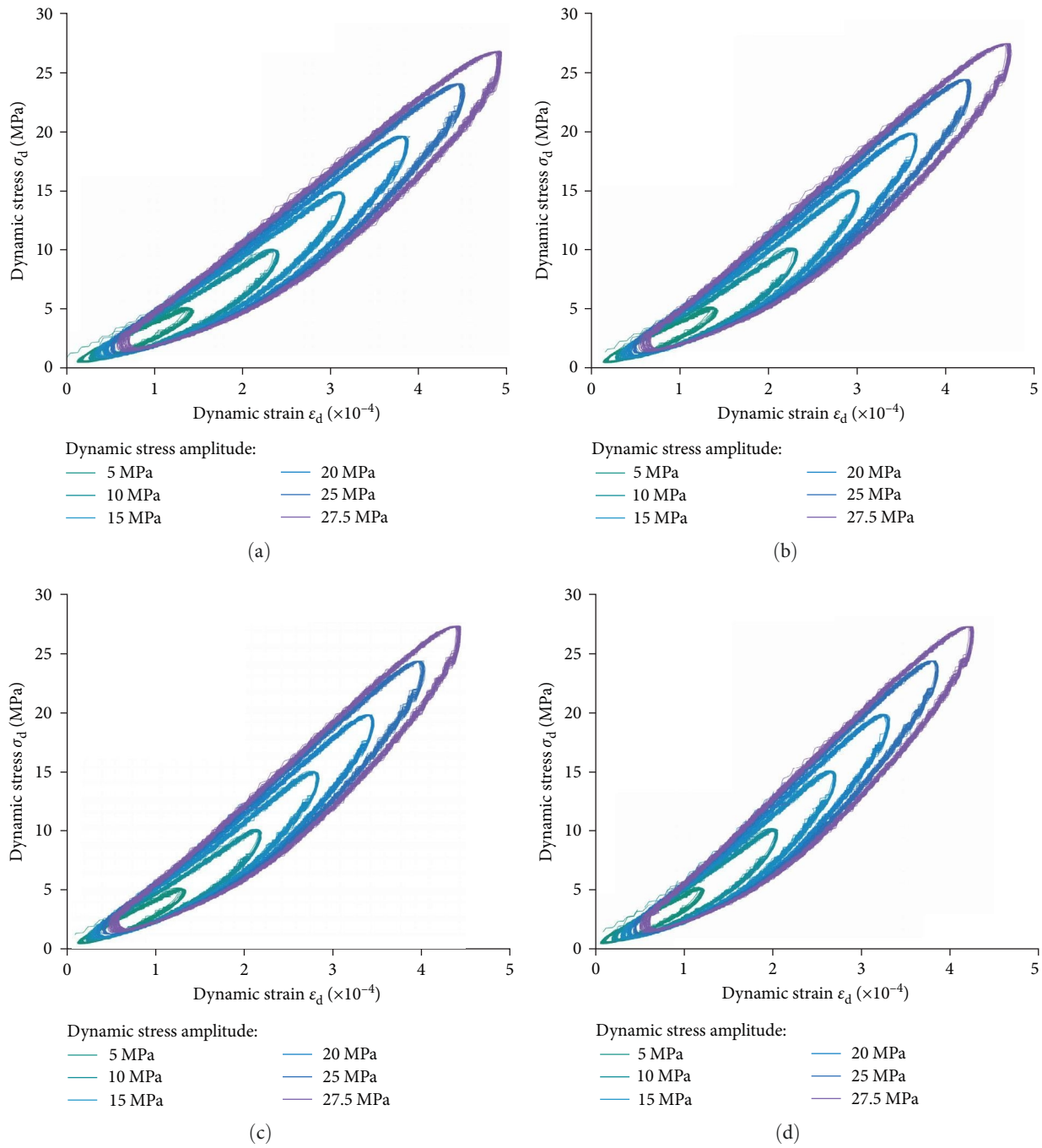

Figure 10: Hysteresis loop diagram with confining pressure: (a) D_{30}5-5, (b) D_{30}5-10, (c) D_{30}5-20, and (d) D_{30}5-30.

particles occurs after the sample is cut, and subsequent adherence of the sample to the adhesive results in inadequate contact. Consequently, the dynamic damping ratio still of the sample tends to increase at the beginning of loading.

4.2.2. Effect of Frequency. Figure 16 shows the variation of the dynamic elastic modulus of the sample with different defect degrees concerning frequency, dynamic stress amplitude, and number of cycles. At a frequency of 20 Hz, the activity within the sample becomes intense. In this case, the test equipment was not able to capture the test data for the sample under the preset values. Hence, the data presented in Figure 16, illustrating dynamic stress amplitudes of 15, 17.5, 20, and 22.5 MPa, are indicative of the collectible dataset. The x-axis above the coordinate axis corresponds to the variation of the dynamic elastic modulus of the sample at a frequency of 20 Hz and different dynamic stress amplitudes. The dynamic elastic modulus of samples with different defect degrees increases with an increasing number of cycles, increasing dynamic stress amplitude and increasing frequency overall. Notably, the variation in dynamic elastic modulus among samples with different defect degrees is

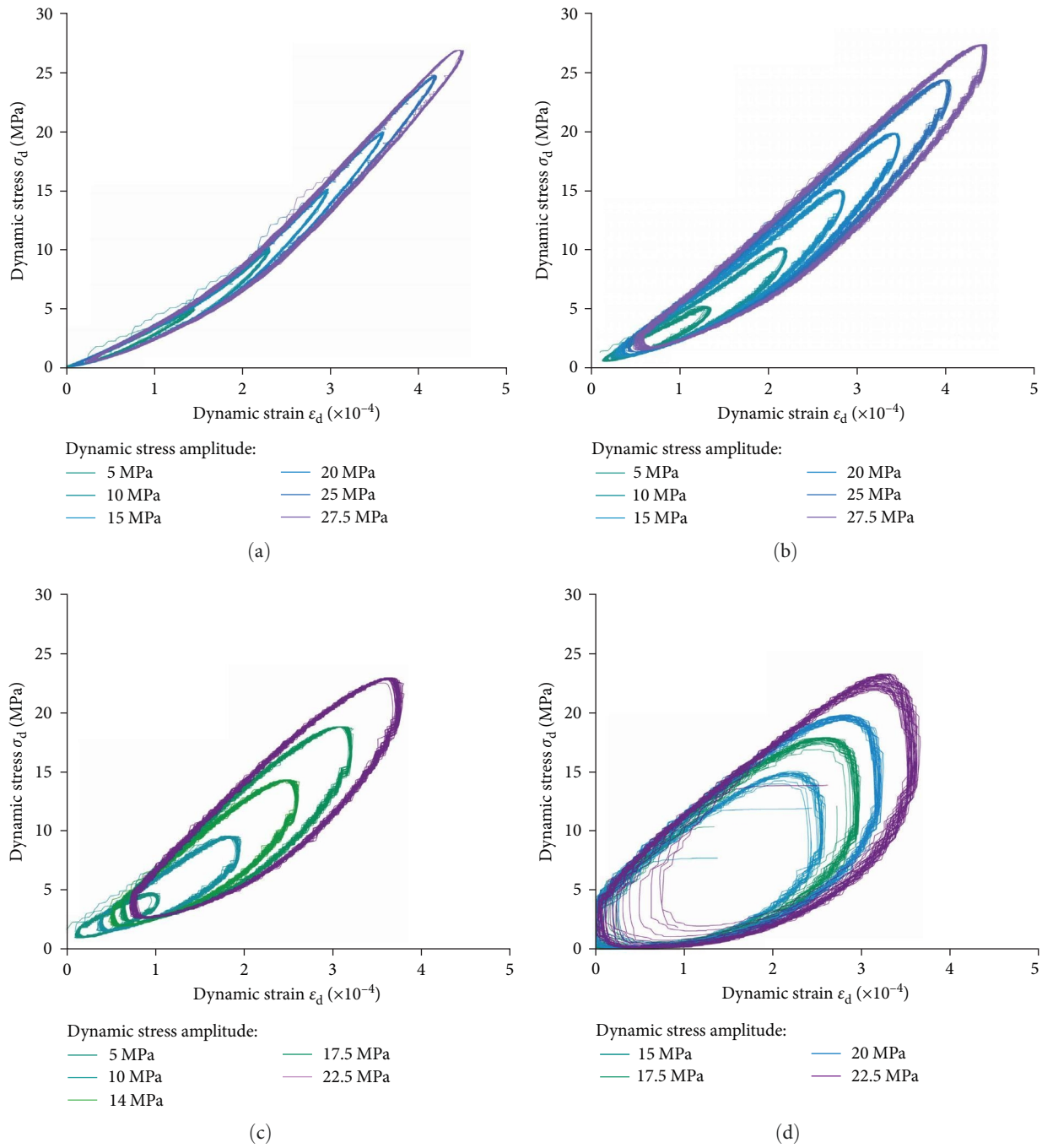

Figure 11: Hysteresis loop diagram with frequency: (a) D_{30}1-20, (b) D_{30}5-20, (c) D_{30}10-20, and (d) D_{30}20-20.

less pronounced within the frequency range of 1–10 Hz compared to the frequency of 20 Hz. Combined with the variation of the hysteresis loop of the samples at high frequencies in Section 3.1.2, we believe that high frequencies have a greater effect on the dynamic properties of the samples. Table 4 shows the growth rate of the dynamic elastic modulus of the samples during the increasing frequency. The dynamic elastic modulus of single jointed 60° sample increased the most.

To observe more directly the variation of the dynamic elastic modulus of the samples with different defect degrees, we show the trend of the average dynamic elastic modulus of the samples with black curves in Figure 17. The dynamic elastic modulus of samples exhibits an increase with increasing frequency, which aligns with the findings of previous studies [11, 12]. We attribute this change to two underlying reasons. On the one hand, as the frequency increases, the mineral particles within the rock undergo repositioning, leading to the closure of cracks due to the deposition of smaller particles [42, 43]. This phenomenon contributes to an overall increase in the dynamic elastic modulus of the sample. On the other hand, as the increase in frequency,

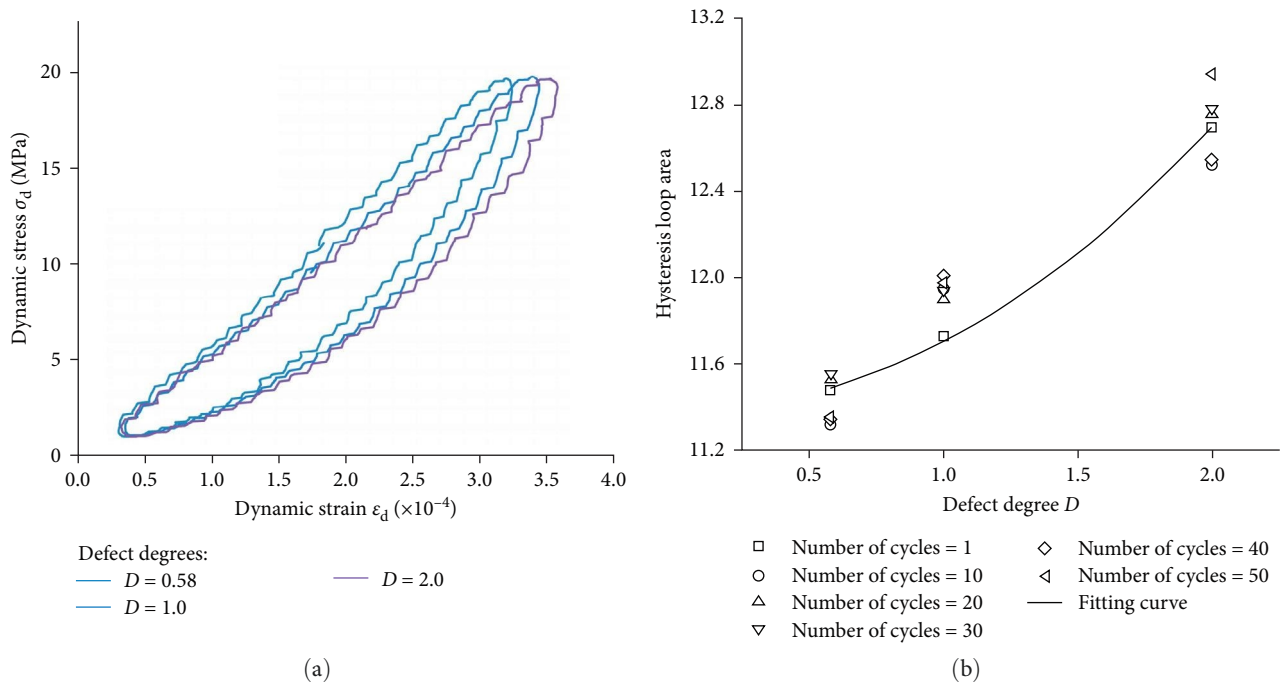

Figure 12: Hysteresis loop diagram hysteresis loop diagram with defect degree: (a) hysteresis loop pattern and (b) Hysteresis loop area.

the viscosity of the fluid between mineral grains inside the granites increases, which causes the dynamic elastic modulus of granites increased [18].

We propose that a quadratic polynomial can describe the relationship between these variables. The trend of the dynamic damping ratio of the normalized samples is depicted by the blue curve in Figure 17. The growth rate of the dynamic damping ratio decreases with increasing dynamic stress amplitude for the single jointed 30° sample and the single jointed 60° sample. The reduction rate of the double jointed 30° sample decreases more at the dynamic stress amplitude of 10–15 MPa, and the reduction rate of the double jointed 30° sample is almost the same as the dynamic stress amplitude of 15–25 MPa.

The variation of the dynamic damping ratio in samples with different defect degrees is illustrated in Figure 18, considering the number of cycles, dynamic stress amplitude, and frequency. At a frequency of 20 Hz, the activity within the sample becomes intense. In this case, the test equipment was not able to capture the test data for the sample under the preset values. Hence, the data presented in Figure 18, illustrating dynamic stress amplitudes of 15, 17.5, 20, and 22.5 MPa, are indicative of the collectible dataset. The x-axis above the coordinate axis corresponds to the variation of the dynamic damping ratio of the sample at a frequency of 20 Hz and different dynamic stress amplitudes. Overall, the dynamic damping ratio of samples with different defect degrees decreases with the increasing number of cycles, decreases with the increasing dynamic stress amplitude, and increases with increasing frequency. The variation curve of the sample dynamic damping ratio is close to a straight line at the frequency of 1–10 Hz. Notably, the curve depicting the variation of the sample's dynamic damping ratio closely approximates a straight line within the frequency range of 1–10 Hz. In contrast, at a frequency of 20 Hz, the dynamic damping ratio demonstrates a wider range of variation compared to the 1–10 Hz frequency range.

To observe more clearly the variation of the dynamic damping ratio for samples with different defect degrees, we show the trend of the average dynamic damping ratio for samples in Figure 19. The average dynamic damping ratio for samples with different defect degrees increases with increasing frequency, which is consistent with Deng et al. [11] and Ni [12]. The variation trend is similar. The dynamic damping ratio of samples with different defect degrees has a substantial increase in frequency 10–20 Hz.

4.2.3. Effect of Dynamic Stress Amplitude. The black curve depicts the variation of the average dynamic elastic modulus of samples with different defect degrees in relation to the increasing dynamic stress amplitude, which is shown in Figure 20. It is evident that the dynamic elastic modulus of the samples exhibits an increase with the rise in dynamic stress amplitude. We consider their relationship as a power function. The blue curve indicates the growth rate of the average dynamic elastic modulus of samples with different defect degrees after normalization in Figure 20. It is worth saying that the growth rate of the dynamic elastic modulus for single jointed 30° samples remains consistent across different confining pressures. In contrast, the growth rate of single jointed 60° samples and double jointed 30° samples is the slowest at a confining pressure of 20 MPa, while it is the fastest at 10 MPa.

The black curve represents the variation of the average dynamic damping ratio of the samples with different defect degrees with increasing dynamic stress amplitude in

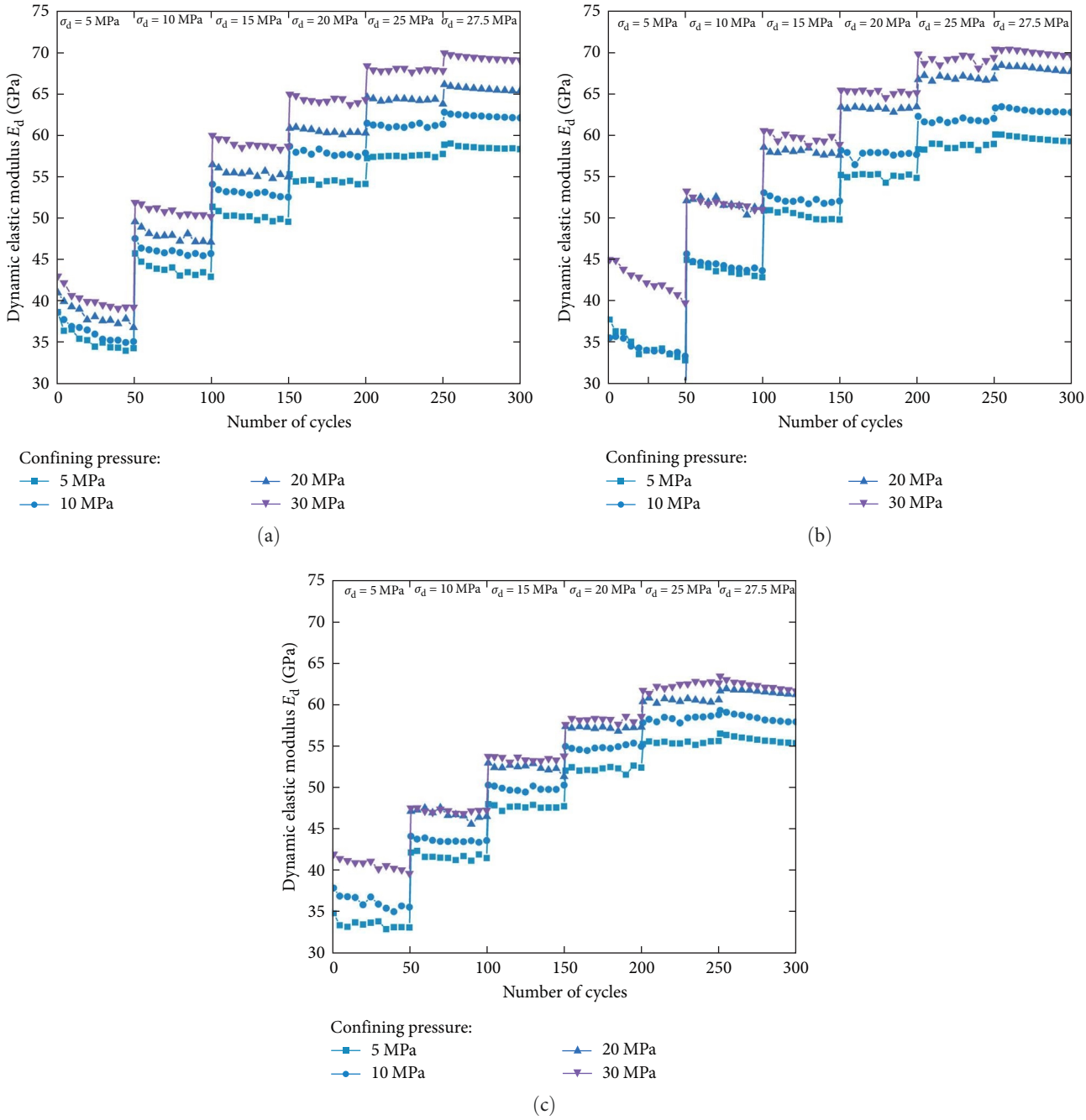

Figure 13: Effect of confining pressure, dynamic stress amplitude and number of cycles on dynamic elastic modulus of samples: (a) single jointed 30° samples, (b) single jointed 60° samples, and (c) double jointed 30° samples.

Table 3: Growth margin of dynamic elastic modulus of samples with confining pressure.

Name	Confining pressure σ (MPa)			
	5–10 Mpa (%)	5–20 Mpa (%)	5–30 Mpa (%)	
Single jointed 30° samples	7.9	12.8	19.4	Maximum increase in dynamic elastic modulus
Single jointed 60° samples	6.8	20.5	27.5	
Double jointed 30° samples	10.9	14.4	24.0	

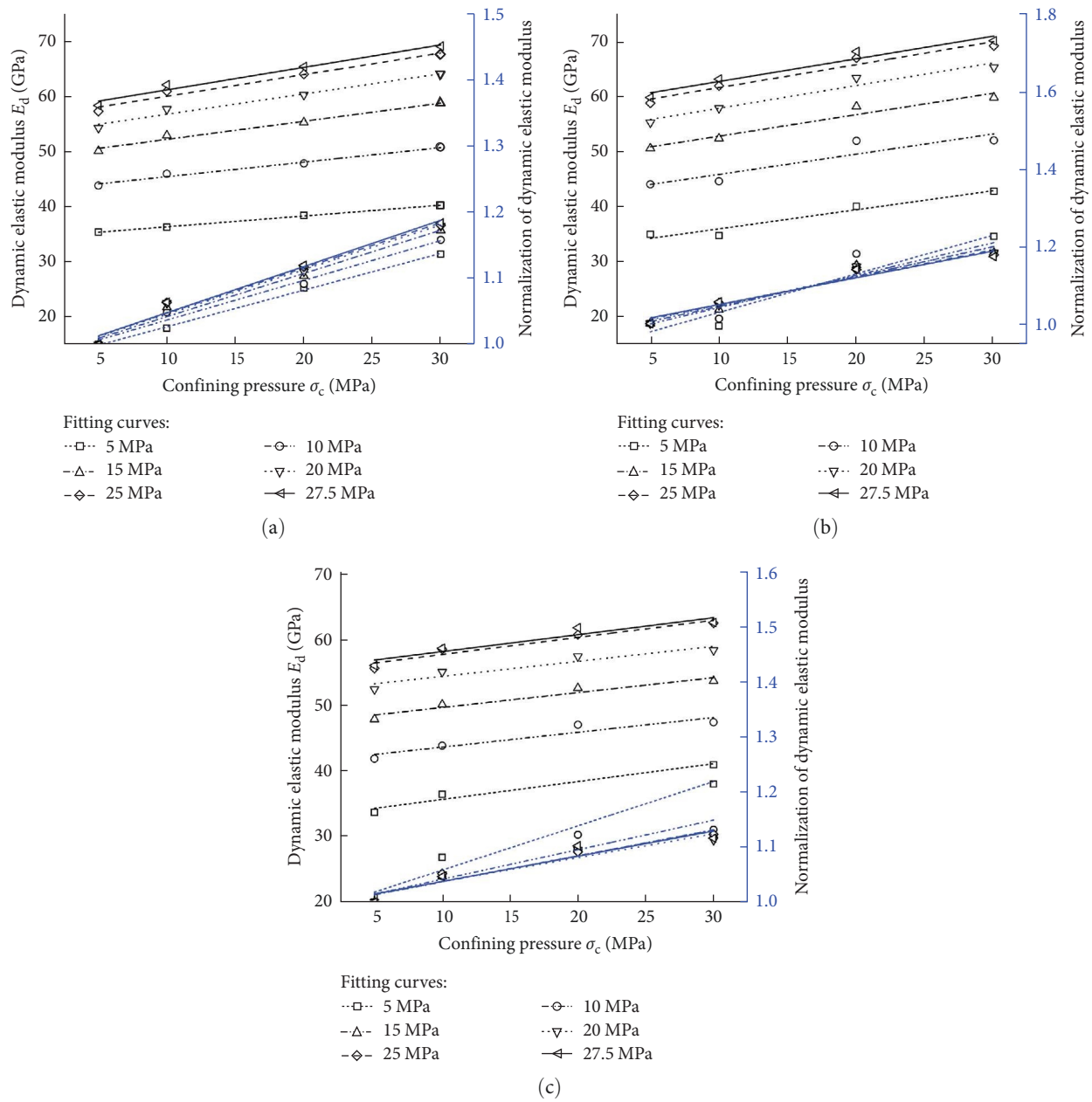

Figure 14: Dynamic elastic modulus of samples with confining pressure: (a) single jointed 30° samples, (b) single jointed 60° samples, and (c) double jointed 30° samples.

Figure 21. It shows that the dynamic damping ratio of the sample increases with increasing the dynamic stress amplitude. We consider their relationship as a power function. Furthermore, the growth rate of samples with different defect degrees exhibits minimal variation.

It is hypothesized that the increase in dynamic stress amplitude compresses the internal mineral particles within the rock. Simultaneously, localized fractures between mineral particles generate additional plastic strain. These factors collectively contribute to an elevation in the dynamic elastic modulus of the sample at the same confining pressure and frequency.

The black curve represents the variation of the average dynamic damping ratio of the samples with different defect degrees with increasing dynamic stress amplitude in Figure 22. There are some missing data points due to the defect degree of the sample affecting the change in activity within the sample during loading, resulting in a different ability of the device to capture samples with different defect degrees. Consequently, the absent data in Figure 22 pertains to both the single jointed 60° sample and the double jointed 60° sample under a dynamic stress amplitude of 5 MPa and a confining pressure of 20 MPa. The observed trend demonstrates that the dynamic damping ratio of the sample

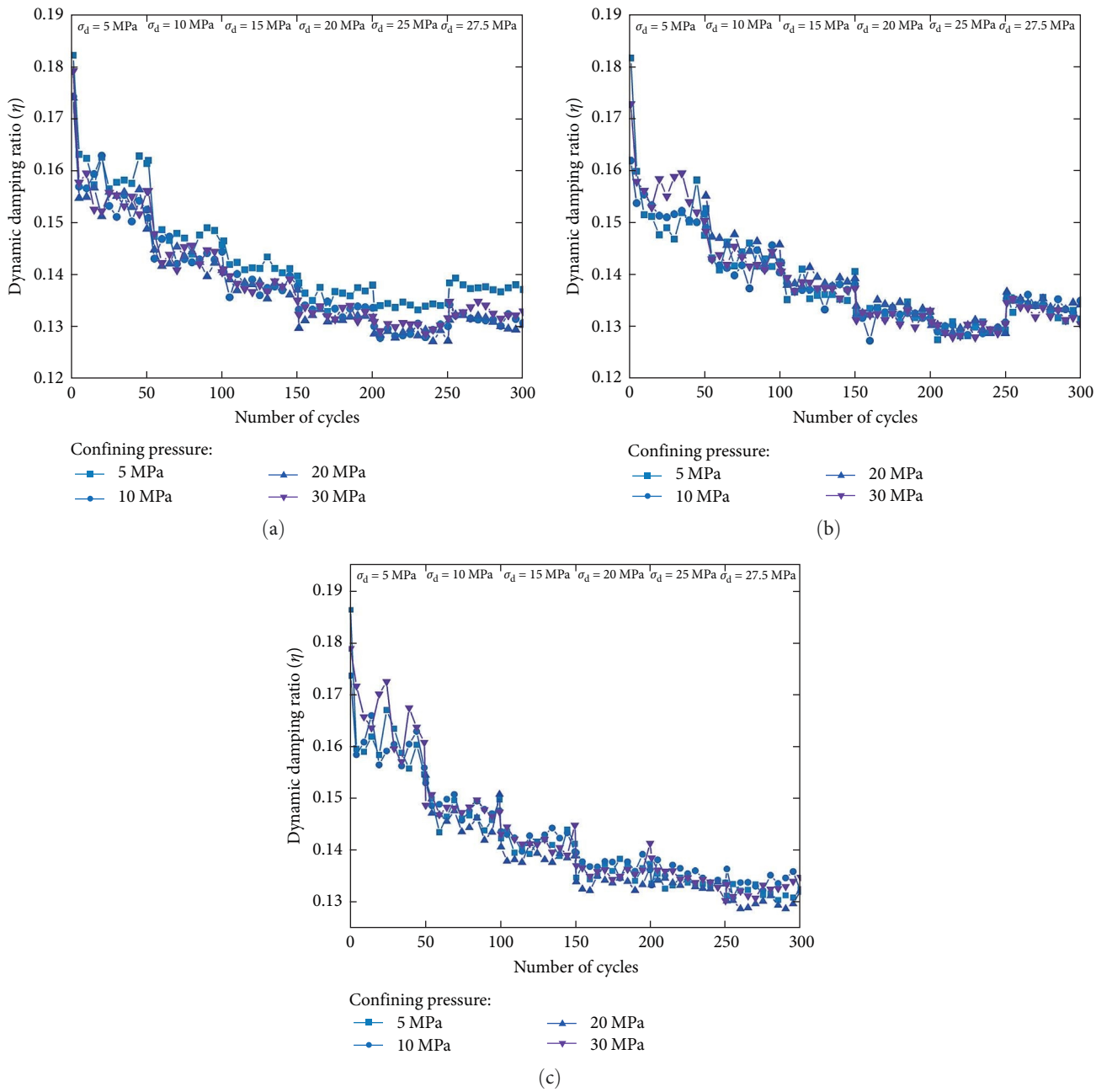

Figure 15: Effect of confining pressure, dynamic stress amplitude and number of cycles on dynamic damping ratio of samples: (a) single jointed 30° samples, (b) single jointed 60° samples, and (c) double jointed 30° samples.

decreases with higher dynamic stress amplitudes. We consider their relationship as a power function. The blue curve indicates the reduction rate of the average dynamic damping ratio of samples with different defect degrees after normalization in Figure 22. Notably, the blue curves of the nodal 30° samples exhibit substantial overlap, indicating a consistent reduction rate. Similar conclusions can also be drawn for single jointed 60° samples. The reduction rate of the dynamic damping ratio of the double jointed 60° sample varies at different confining pressures, but the range of variation is not large.

The black curve represents the variation of the average dynamic damping ratio of the samples with different defect degrees with increasing dynamic stress amplitude in Figure 23. There are some missing data points due to the defect degree of the sample affecting the change in activity within the sample during loading, resulting in a different ability of the device to capture samples with different defect degrees. Consequently, the absent data in Figure 23 pertains to both the single jointed 60° sample and the double jointed 60° sample under a dynamic stress amplitude of 5 MPa and a loading frequency of 5 Hz. Owing to the intricacy of the test variable configuration, certain combinations of test variables render the equipment incapable of capturing the corresponding data, resulting in missing data in Figure 23. It shows that the dynamic damping ratio of the sample decreases with increasing the dynamic

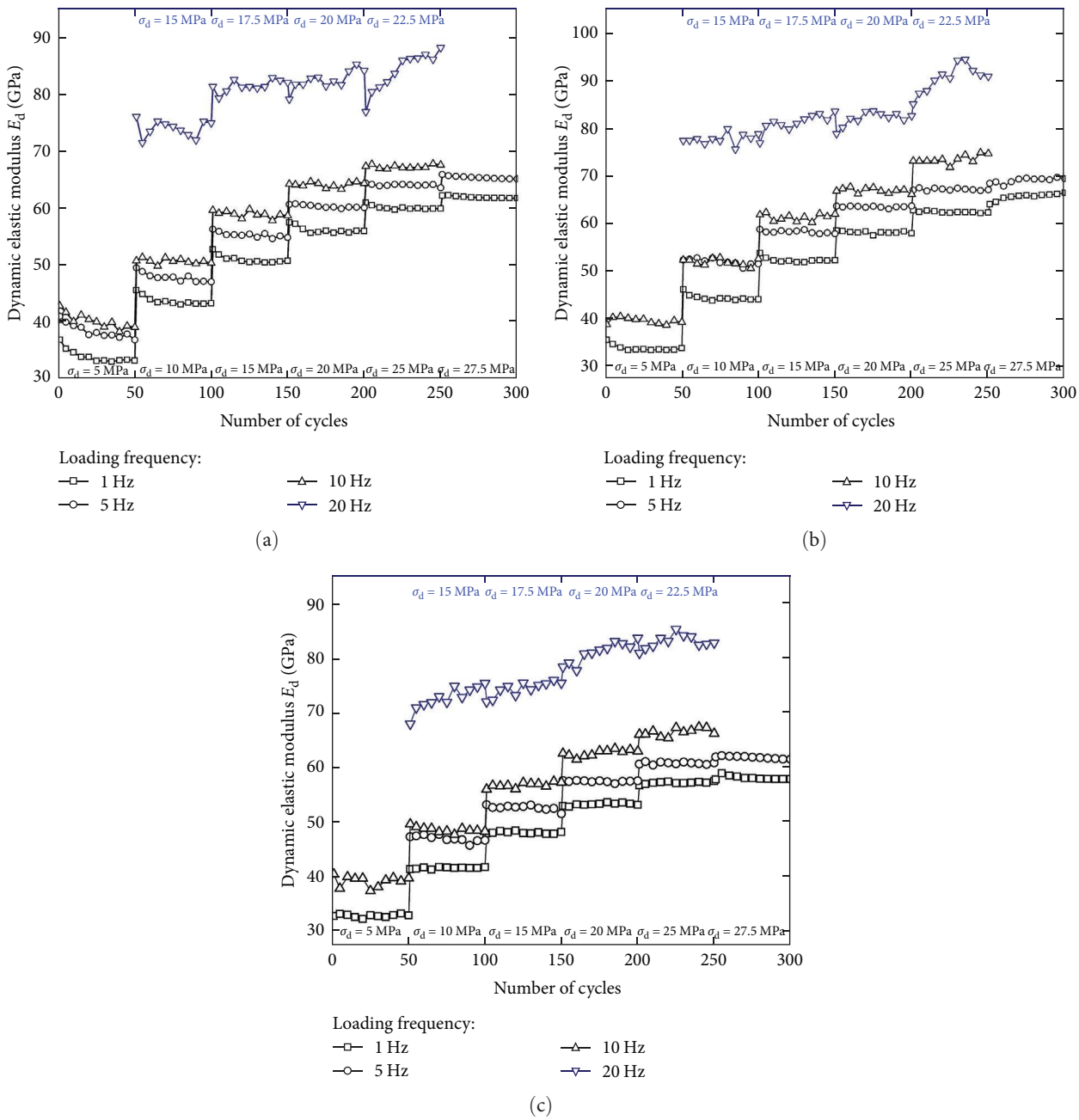

Figure 16: Effect of frequencies, dynamic stress amplitude and number of cycles on dynamic elastic modulus of samples: (a) single jointed 30° samples, (b) single jointed 60° samples, and (c) double jointed 30° samples.

Table 4: Growth margin of dynamic elastic modulus of samples with frequency.

Name	Frequency f (Hz)			
	1–5 Hz (%)	1–10 Hz (%)	1–20 Hz (%)	
Single jointed 30° samples	15.4	21.7	74.1	Maximum increase in dynamic elastic modulus
Single jointed 60° samples	20.4	20.4	80.6	
Double jointed 30° samples	14.4	23.4	80.3	

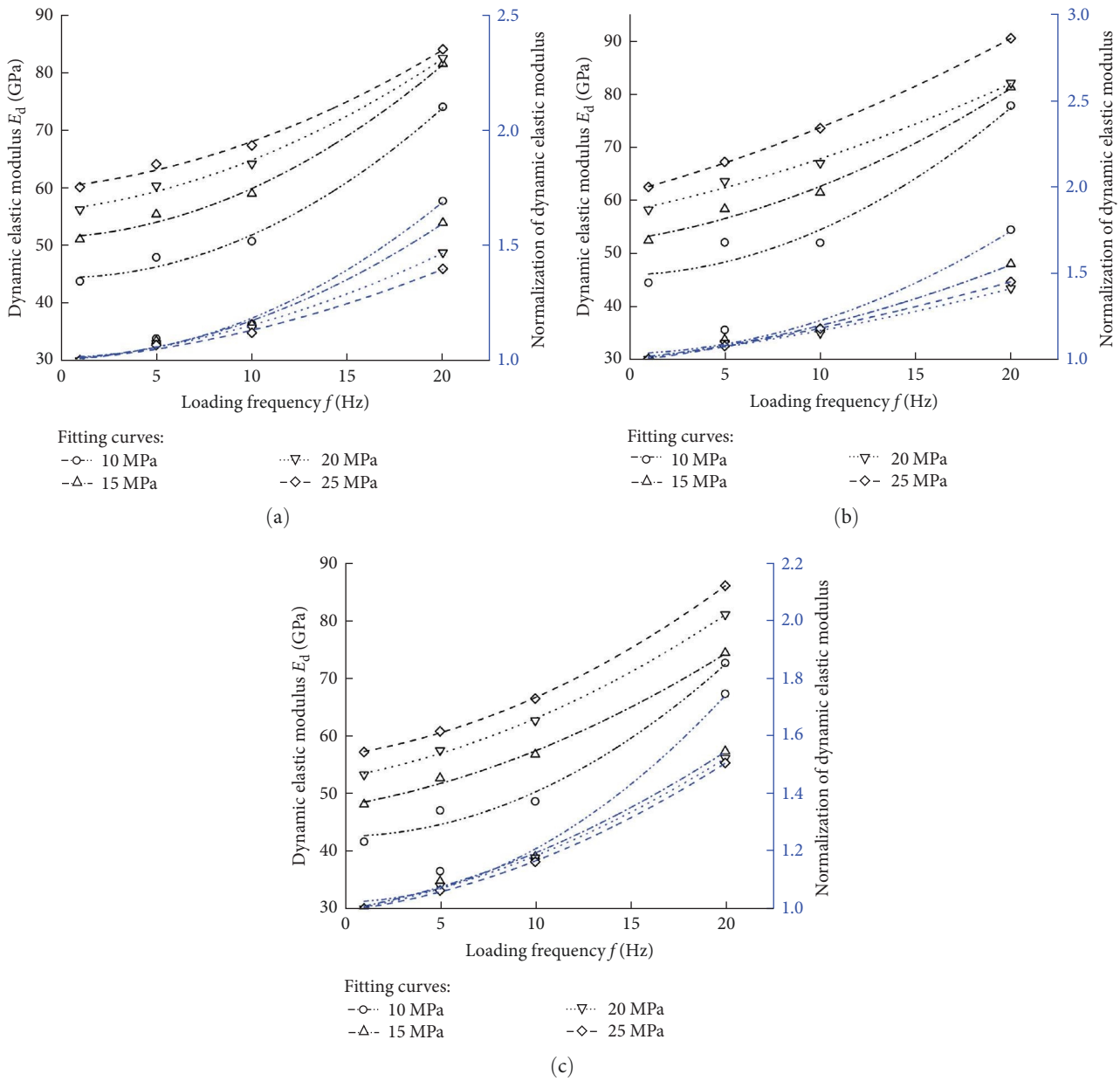

Figure 17: Dynamic elastic modulus of samples with frequencies: (a) single jointed 30° samples, (b) single jointed 60° samples, and (c) double jointed 30° samples.

stress amplitude overall. We consider their relationship as a power function. The blue curve indicates the reduction rate of the average dynamic damping ratio of samples with different defect degrees after normalization in Figure 23. We found more normalized data that were not on the curve, indicating that the data were more discrete. In this case, we believe that the dynamic stress amplitude has a small effect on the reduction rate of the dynamic damping ratio of the sample compared to the confining pressure and loading frequency.

Some scholars obtained a similar conclusion by using sandstone [44], marble [45], and fine sandstone [46]. However, the conclusion of He et al.'s [47] experiment is contrary to our conclusion. He found that the dynamic damping ratio of the rock decreased with increasing dynamic stress amplitude. After comparison, we found that the rocks were used in He et al.'s [47] experiment are soft rock, and granite belongs to hard rock. For this, we believe that the dynamic damping ratio of rocks has a relationship with the kinds of rock.

4.2.4. Effect of Number of Cycles. Figure 24 depicts the dynamic elastic modulus variation with an increasing number of cycles under different confining pressures. It is evident that the dynamic elastic modulus of samples with diverse defect degrees exhibits a decrease as the number of cycles increases. It indicated that the irreversible deformation of the samples subjected to cyclic loading was developing. The conclusion is consistent with Wang et al.'s [48] and Peellage et al.'s [40] results.

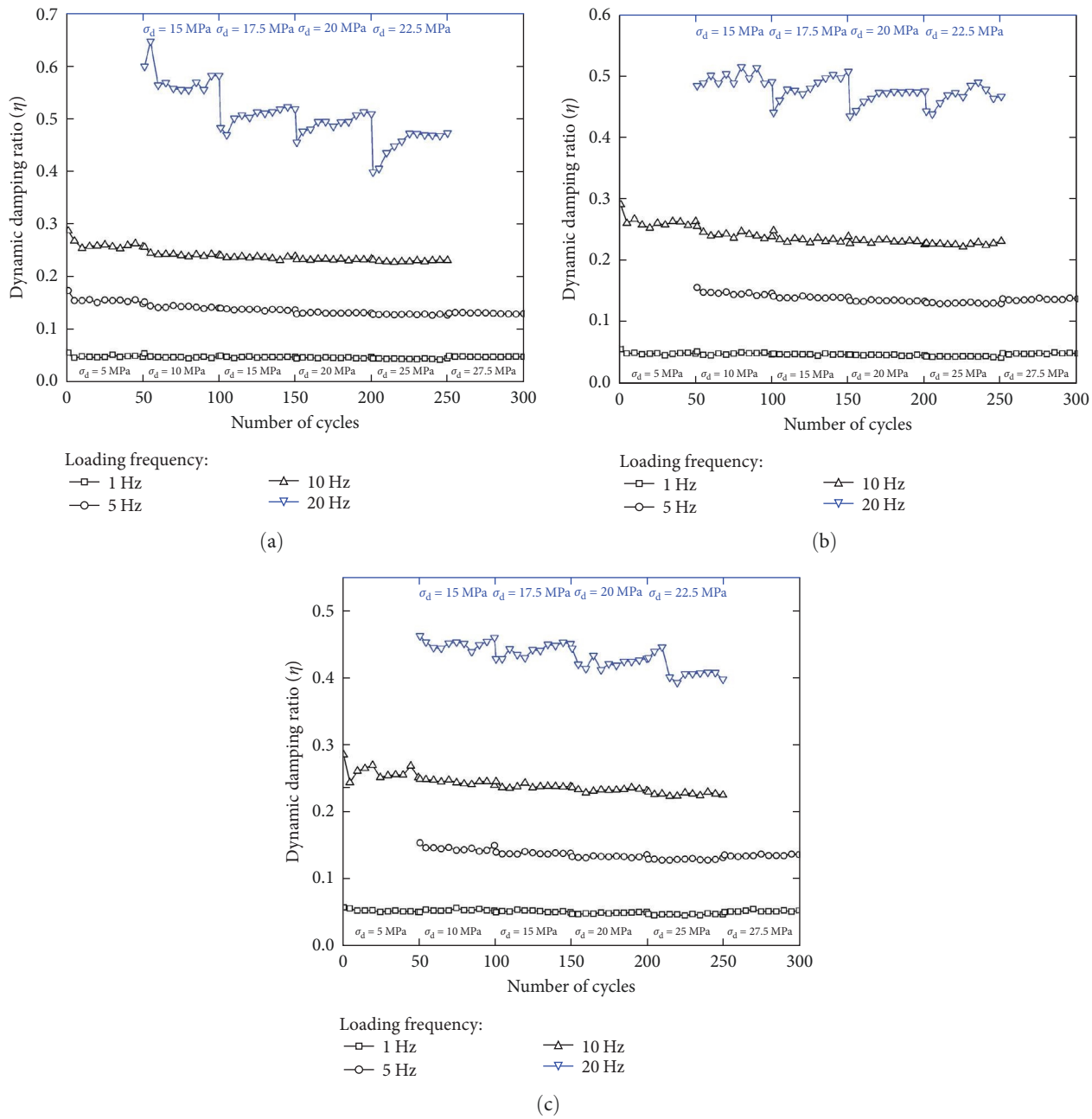

Figure 18: Effect of frequencies, dynamic stress amplitude and number of cycles on dynamic damping ratio of samples: (a) single jointed 30° samples, (b) single jointed 60° samples, and (c) double jointed 30° samples.

Figure 25 shows the variation of the dynamic damping ratio with an increasing number of cycles at different loading frequencies. The dynamic damping ratio of samples with distinct defect degrees exhibits a decrease as the number of cycles increases, accompanied by significant fluctuations. It indicates that the energy change inside the sample is more drastic.

Figure 26 shows the trend of the dynamic elastic modulus with an increasing number of cycles for samples with different defect degrees. The dynamic damping ratio of the sample exhibits a mixed behavior, with alternating increments and decrements throughout the cycling process. However, the overall trend indicates a decrease in the dynamic damping ratio as the number of cycles increases. According to Wang et al. [49] and Liu et al. [9], the irreversible strain is generated in the first few cycles, and storing lower levels of elastic energy requires higher energy dissipation, so a higher dynamic damping ratio can be seen in the first few cycles, and then gradually decreased to stability.

Figure 27 shows the trend of the dynamic damping ratio with an increasing number of cycles for samples with different defect degrees. The comprehensive trend of the dynamic damping ratio for the sample indicates a marginal decrease with an increase in the number of cycles, indicating a

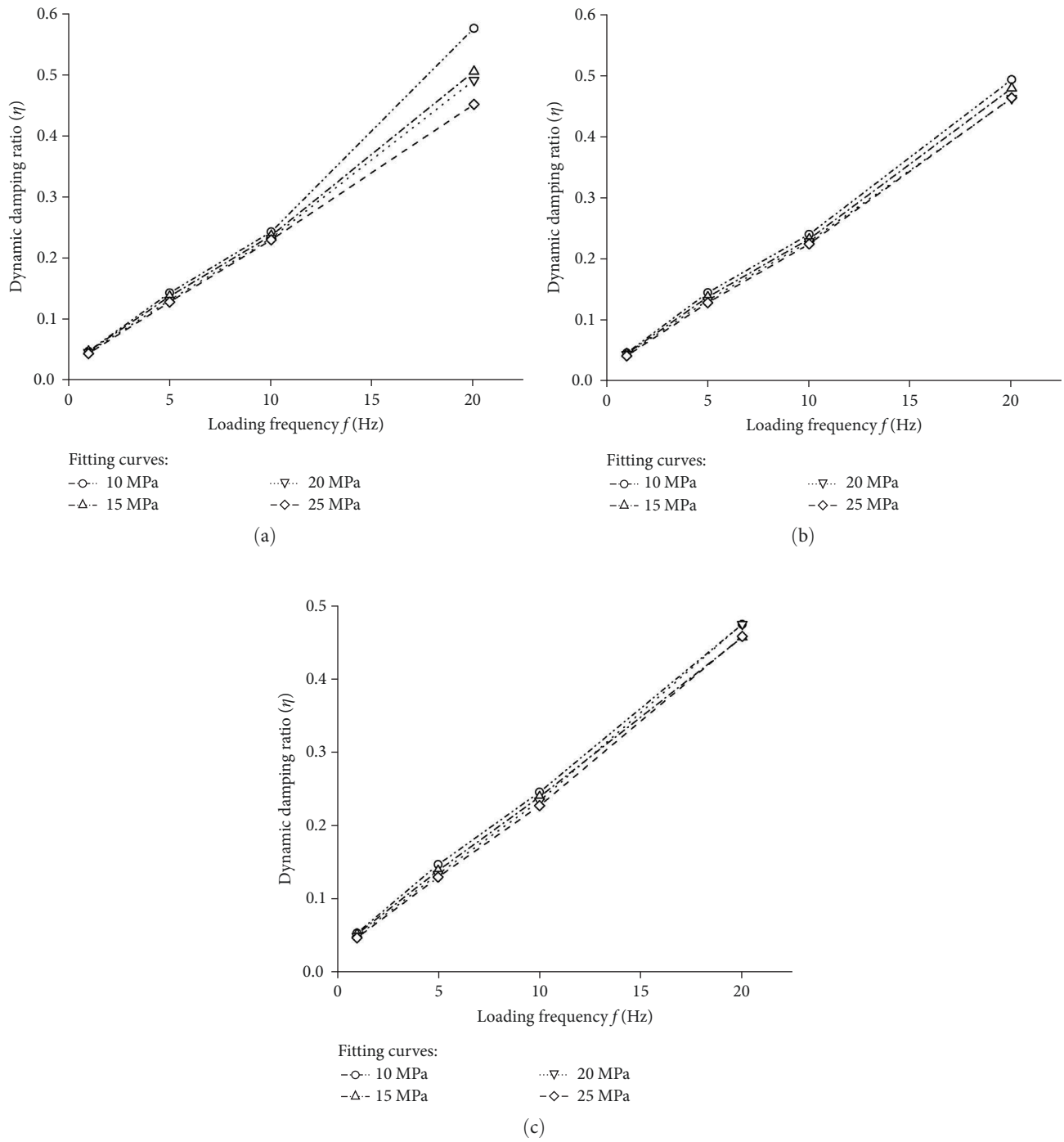

Figure 19: Dynamic damping ratio of samples with frequencies: (a) single jointed 30° samples, (b) single jointed 60° samples, and (c) double jointed 30° samples.

relatively limited sensitivity of the dynamic damping ratio to the variations in the number of cycles, especially at lower frequencies.

4.2.5. Effect of Defect Degree. Figure 28 depicts the variation of the dynamic elastic modulus of the samples under different load combinations. To better compare the effect of the defect degree on the dynamic elastic modulus of the samples, we include the data of the intact samples obtained from previously conducted tests [34] in Figure 28. The findings demonstrate a decrease in the dynamic elastic modulus of the sample as the defect factor increases. Figure 29 shows the effect of the sample after loading. It is difficult to perform the crack distribution under nondestructive loading because

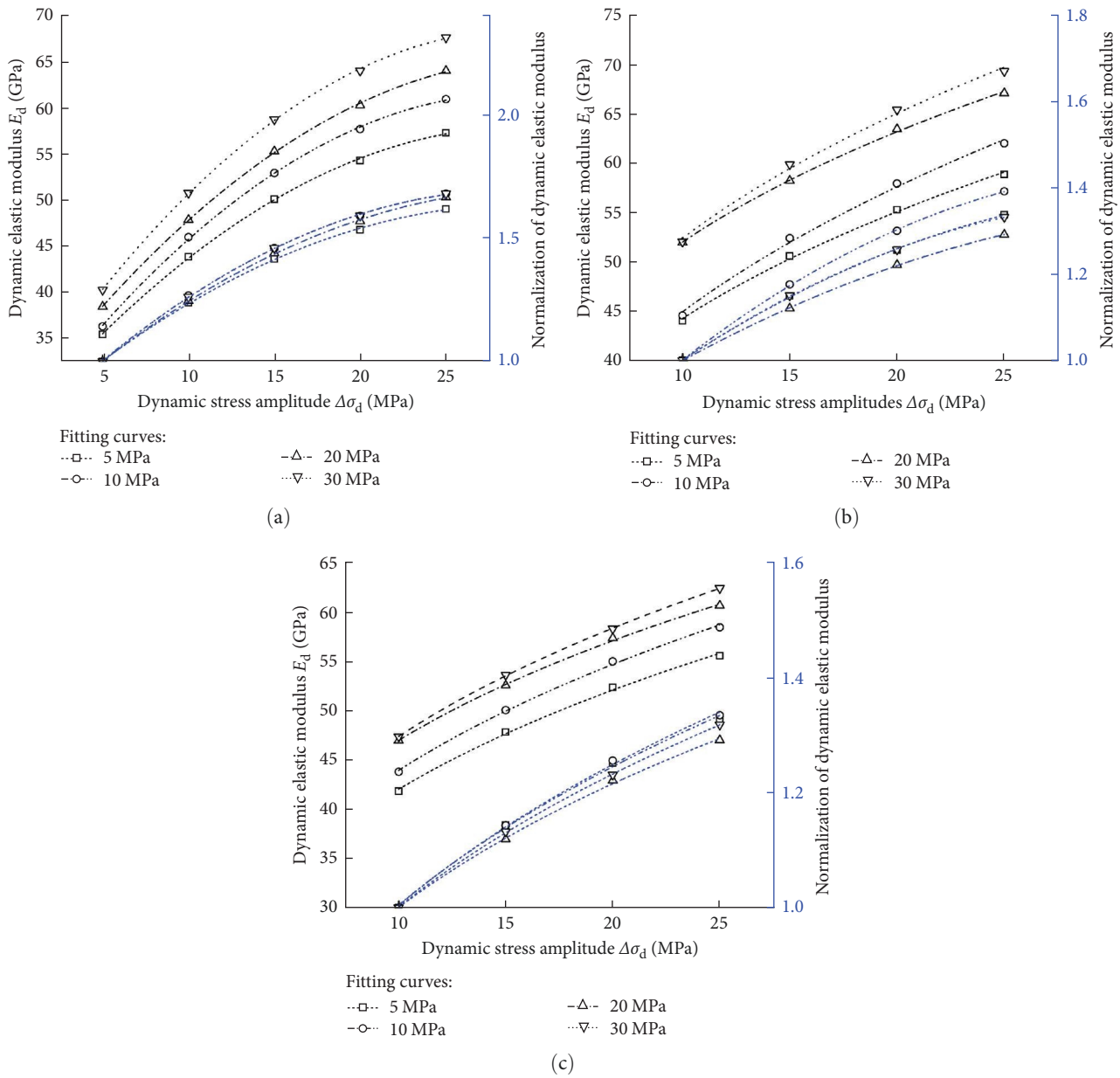

Figure 20: Dynamic elastic modulus of samples with dynamic stress amplitude and confining pressure: (a) single jointed 30° samples, (b) single jointed 60° samples, and (c) double jointed 30° samples.

the loaded jointed samples are damaged (Figure 29(a)). Therefore, we use the intact sample (Figure 29(b)) to combine the analysis.

In Figure 29(b), the cracks observed in the intact rock during loading predominantly exhibit a transverse orientation. Since the joint of the single jointed 60° sample is at 60° to the horizontal plane, it makes the prefabricated jointed and the transverse cracks generated by cyclic loading do not easily overlap, resulting in a smaller reduction in sample stiffness. The joint of the single jointed 30° sample is at 30° to the horizontal plane, which tends to overlap with the newly generated cracks in loading, further weakening the stiffness of the sample. For a double jointed 30° sample, the area formed between the joints cannot bear too much stress. The two joints mean that they will overlap more with the newly created crack. It resulted in a higher decrease in the dynamic elastic modulus of the double jointed 30° sample.

Figure 30 presents the variation of the dynamic damping ratio of the samples under different loading combinations. To better compare the effect of the defect degree on the dynamic damping ratio of the samples, we include the data of the intact samples obtained from previously conducted tests [34] in Figure 30. It demonstrates that as the defect degree increases, the dynamic damping ratio of samples increases. Our interpretation is based on the understanding that the reduced stiffness resulting from the presence of joints makes the sample more susceptible to crack formation during loading. The increase in energy consumption during crack generation leads to an increase in the sample's dynamic damping ratio.

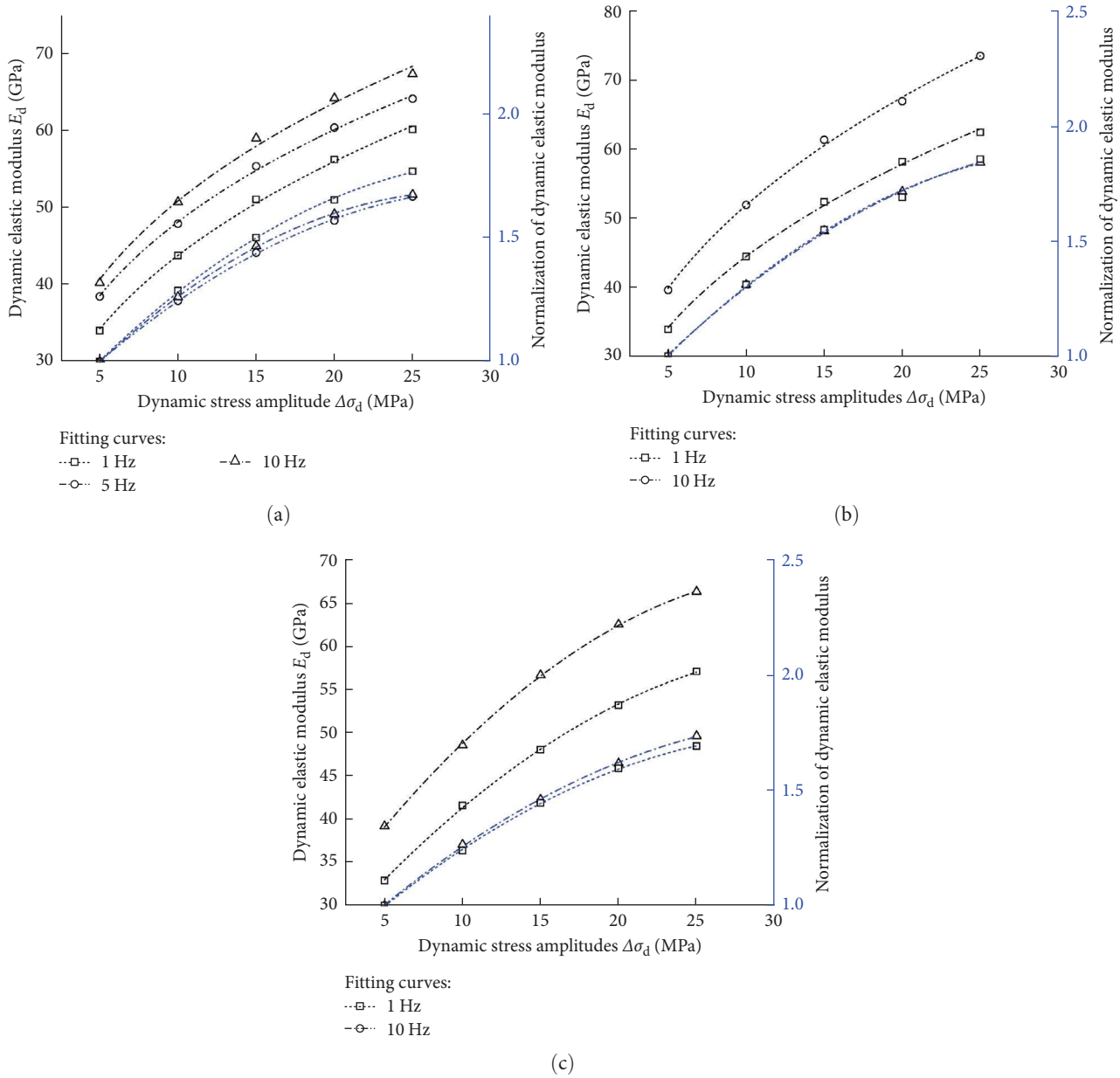

Figure 21: Dynamic elastic modulus of samples with dynamic stress amplitude and frequency: (a) single jointed 30° samples, (b) single jointed 60° samples, and (c) double jointed 30° samples.

5. Dynamic Response Model

5.1. Model Establishment. Duncan–Chang model is the most classical one of the nonlinear elastic models [50], which can reflect the mechanical behavior of the rock well. Many researchers have used the Duncan–Zhang model to conduct research on the mechanical behavior of rocks and have obtained good results [51–53]. The frequencies we set in our experiments are 1–20 Hz, and we consider the samples in quasi-static loading. Therefore, combining the loading characteristics and the advantages of the model, we chose the Duncan–Chang model to carry out our study. Moreover, the acquired Duncan–Chang model is employed for inverse analysis to ascertain the working condition of the target rock. With the objective of enhancing the accuracy of the inverse analysis results, we have formulated distinct Duncan–Chang models tailored to samples with different degrees of defects.

The following relationship between dynamic stress and dynamic strain in the Duncan–Chang model is as follows:

$$\sigma_d = \frac{\Delta\varepsilon_d}{a + b\Delta\varepsilon_d}, \tag{4}$$

where σ_d is dynamic stress level. $\Delta\varepsilon_d$ is dynamic strain amplitude, a and b are test parameters.

Figure 31 shows the results of fitting samples with different defect degrees with Equation (4). Most of the data are on

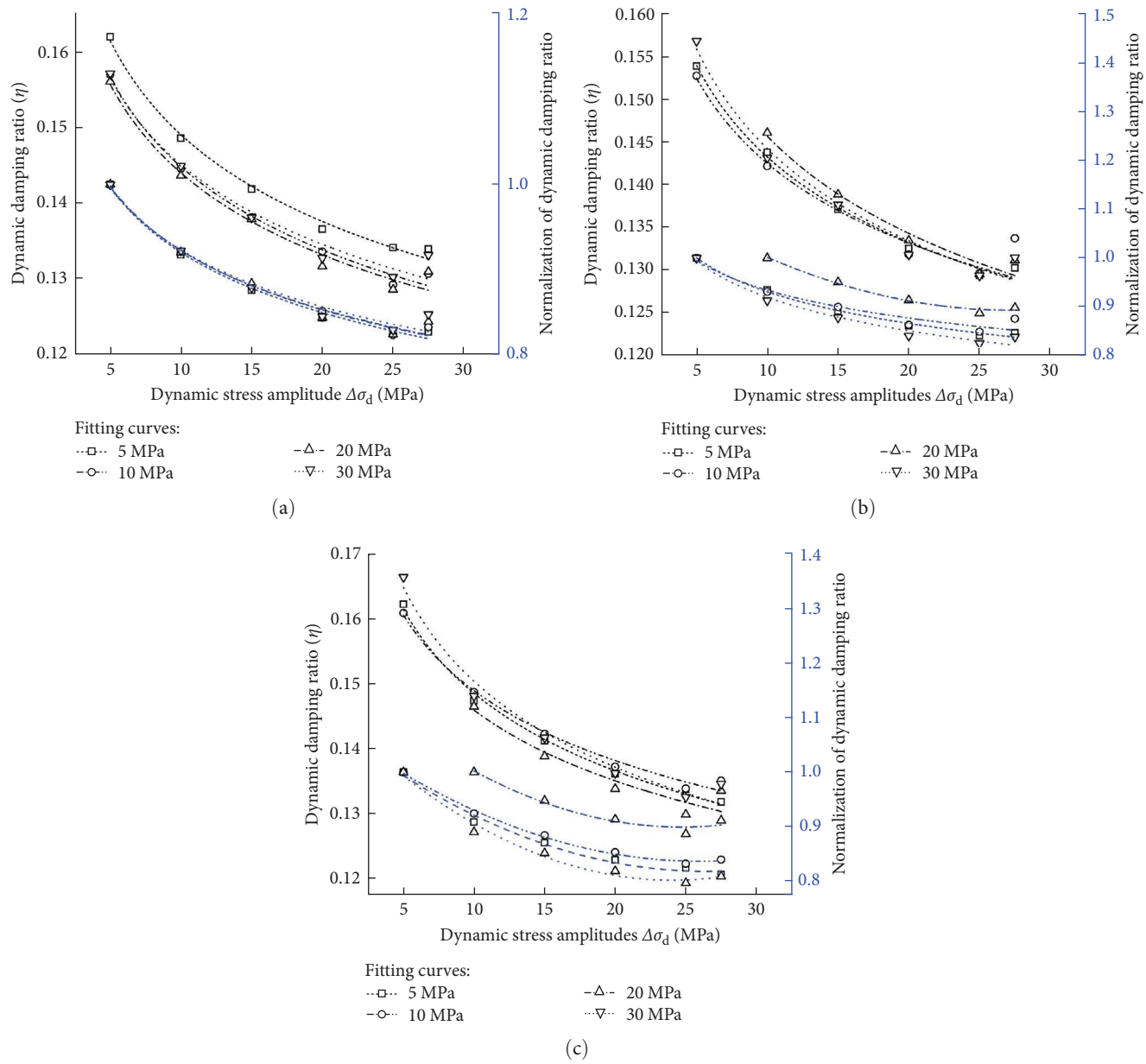

Figure 22: Dynamic damping ratio of samples with dynamic stress amplitude and confining pressure: (a) single jointed 30° samples, (b) single jointed 60° samples, and (c) double jointed 30° samples.

the fitting curve. It indicates that Equation (4) can reflect the relationship between dynamic stress and dynamic strain amplitude.

To facilitate obtaining the model parameters a and b related to the confining pressure and frequency, we transform Equation (4) into the following relationship:

$$\frac{\Delta\varepsilon_d}{\sigma_d} = a + b\Delta\varepsilon_d, \tag{5}$$

where σ_d is dynamic stress level. $\Delta\varepsilon_d$ is dynamic strain amplitude, a and b are test parameters.

Figure 32 shows the decrease ratio of dynamic strain amplitude to dynamic stress with increasing dynamic strain amplitude. However, most of the data are not on the fitted curve at frequencies of 1–10 Hz, indicating that Equation (5) is not suitable for fitting the data. Through the analysis of the data, we prefer that the ratio of dynamic strain amplitude to dynamic stress and dynamic strain amplitude have a quadratic polynomial relationship. Therefore, we improved the Duncan–Chang model as the following formula:

$$\sigma_d = \frac{\Delta\varepsilon_d}{a + b\Delta\varepsilon_d + c\Delta\varepsilon_d^2}, \tag{6}$$

$$\frac{\Delta\varepsilon_d}{\sigma_d} = a + b\Delta\varepsilon_d + c\Delta\varepsilon_d^2, \tag{7}$$

where σ_d is dynamic stress level. $\Delta\varepsilon_d$ is dynamic strain amplitude, a, b, and c are test parameters.

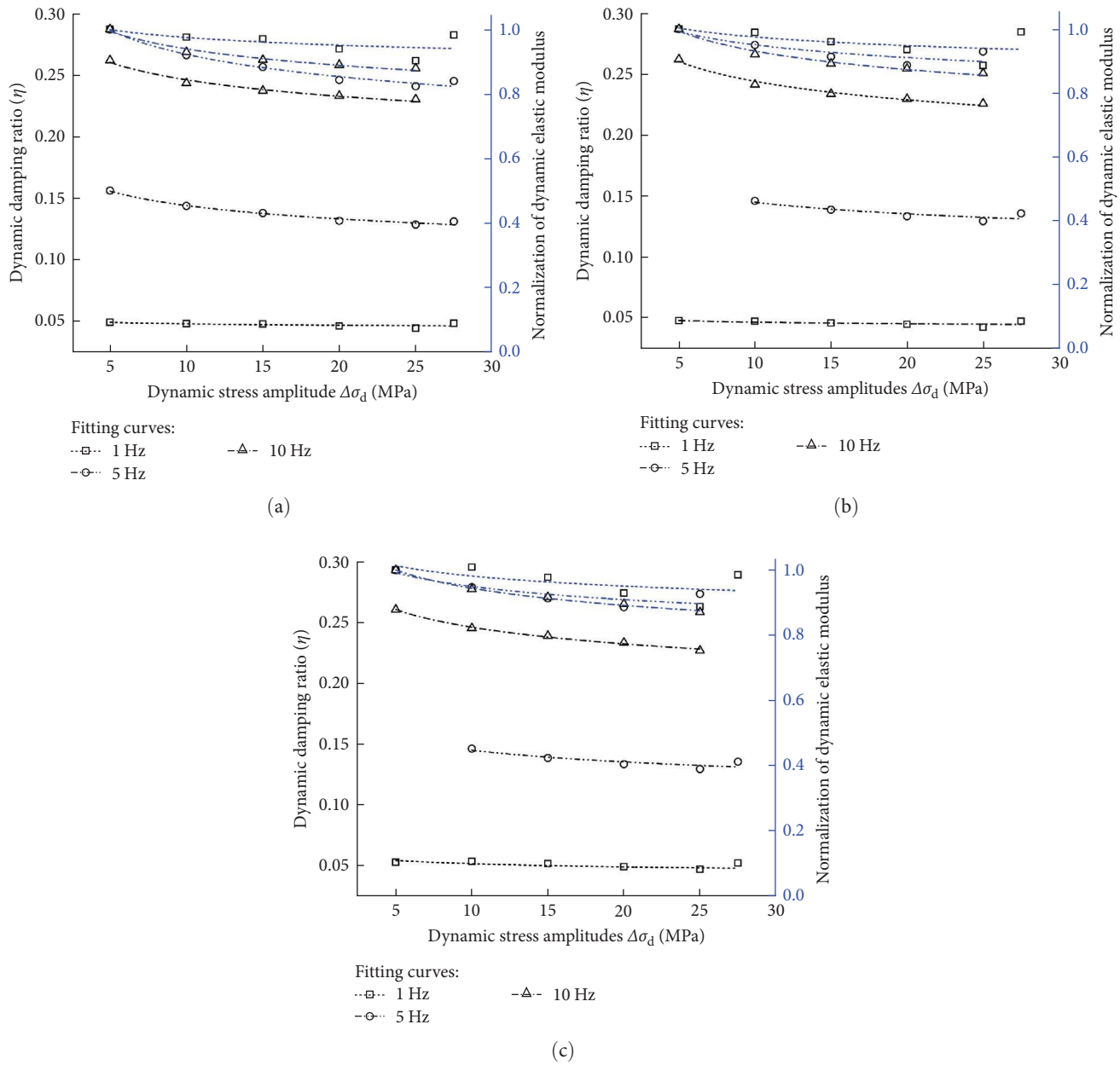

Figure 23: Dynamic damping ratio of samples with dynamic stress amplitude and frequency: (a) single jointed 30° samples, (b) single jointed 60° samples, and (c) double jointed 30° samples.

5.2. Influence of Confining Pressure. Figure 33 displays the outcomes of fitting Equation (6) to depict the relationship between dynamic strain and dynamic stress at confining pressure. The obtained results show that as the dynamic stress increased, the dynamic strain increased. At the same dynamic stress, the dynamic strain in the sample increases by decreasing the confining pressure. The data points align closely with the fitting curve, indicating that Equation (6) is suitable in this test.

Figure 34 presents the outcomes of fitting Equation (7) to establish a relationship between the ratio of dynamic strain amplitude to dynamic stress and dynamic strain. The ratio of dynamic strain amplitude to dynamic stress decreases as the dynamic stress amplitude increases. The correlation coefficients of the fitting formulas all reach 0.99, which indicates that the improved Duncan–Chang model can well express the mechanical properties of the sample during loading. It also shows that our guesses are reasonable.

Table 5 shows the experimental parameters *a*, *b*, and *c* in relation to the variation of the confining pressure. The parameter *a* is linear with the confining pressure for samples with different defect degrees. Parameters *b* and *c* of the single jointed 30° sample are related to the confining pressure as a power function. Parameters *b* and *c* of the single jointed 60° sample have a quadratic polynomial relationship with the confining pressure.

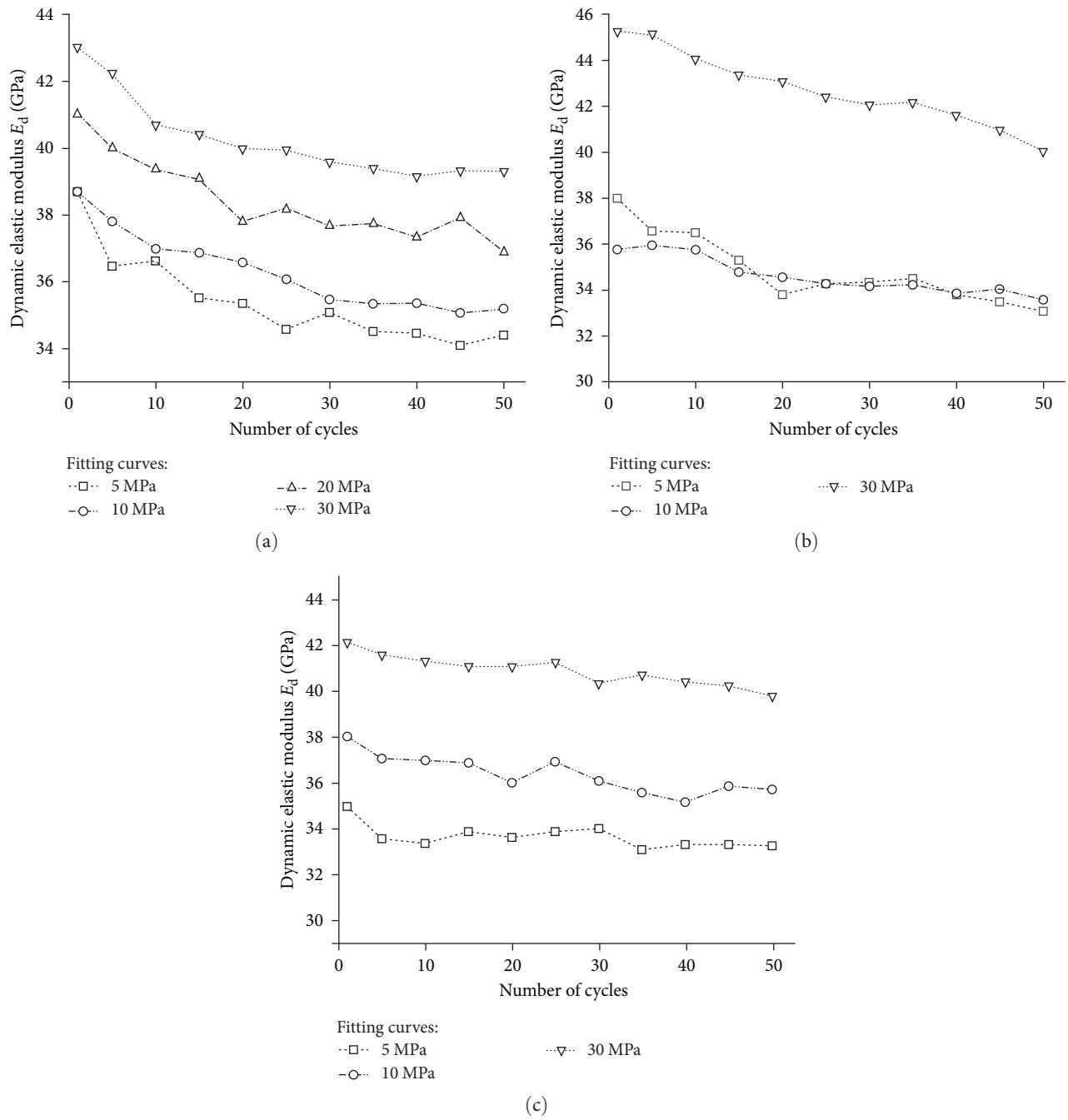

Figure 24: Dynamic elastic modulus of samples with number of cycles and confining pressure: (a) single jointed 30° samples, (b) single jointed 60° samples, and (c) double jointed 30° samples.

Parameters b and c of double jointed 30° sample are related to the confining pressure as a power function.

5.3. Influence of Loading Frequency. Figure 35 displays the outcomes of fitting Equation (6) to depict the relationship between dynamic strain and dynamic stress at loading frequency. The obtained results show that as the dynamic stress increased, the dynamic strain increased. At the same dynamic stress, the dynamic strain in the sample increases by decreasing the frequency. The data points align closely with the fitting curve, indicating that Equation (6) is suitable in this test.

Figure 36 presents the outcomes of fitting Equation (7) to establish a relationship between the ratio of dynamic strain amplitude to dynamic stress and dynamic strain. The ratio of dynamic strain amplitude to dynamic stress decreases as the dynamic stress amplitude increases. At frequencies ranging from 1 to 10 Hz, the correlation coefficient of the formula reaches 0.98, indicating that the model accurately captures the mechanical behavior of the sample. However, the formula correlation coefficient is generally low at a frequency of 20 Hz, reaching only 0.94 for a single jointed 30° sample. This suggests that higher frequencies exert a greater

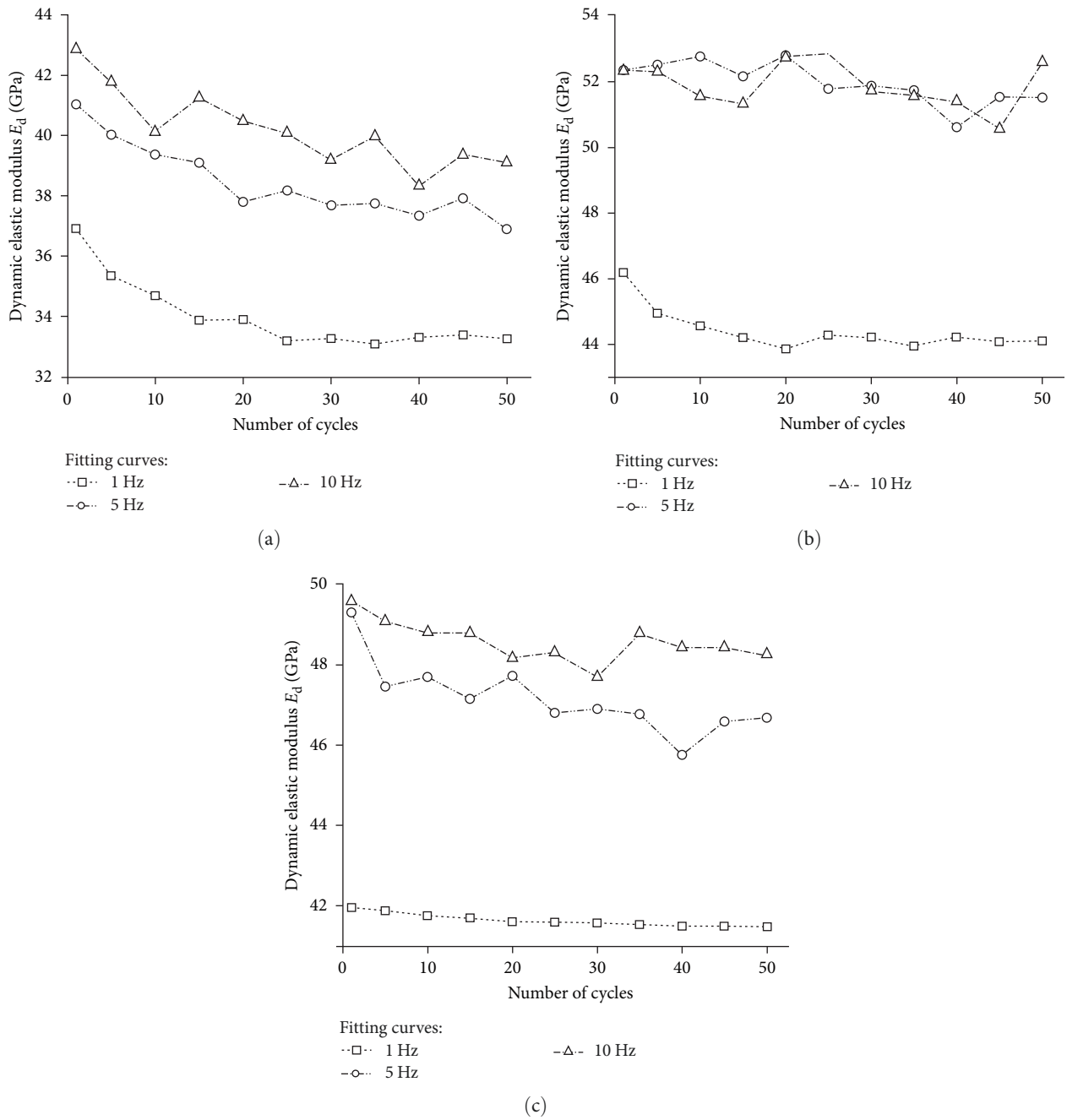

Figure 25: Dynamic elastic modulus of samples with number of cycles and frequency: (a) single jointed 30° samples, (b) single jointed 60° samples, and (c) double jointed 30° samples.

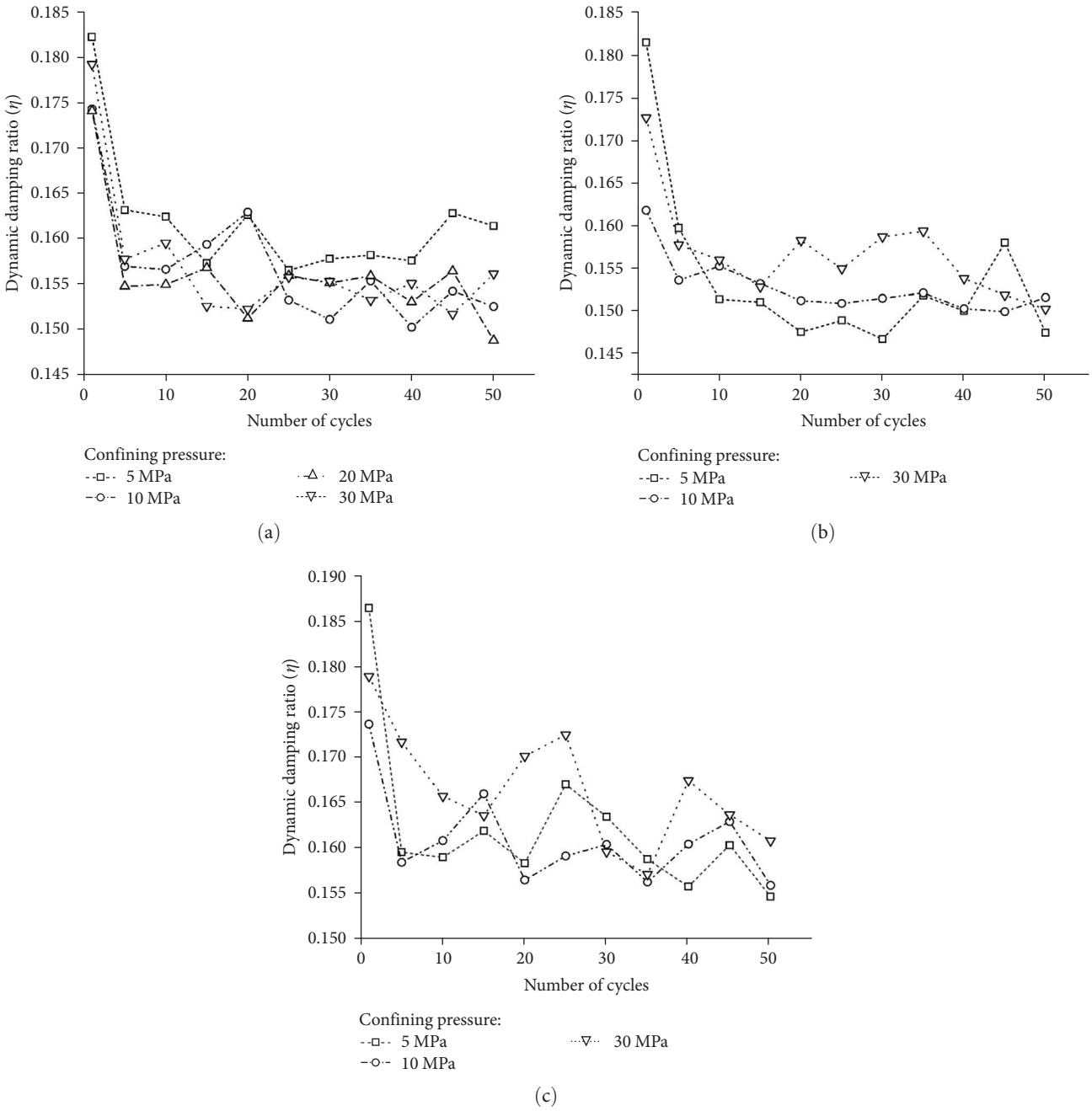

Figure 26: Dynamic damping ratio of samples with number of cycles and confining pressure: (a) single jointed 30° samples, (b) single jointed 60° samples, and (c) double jointed 30° samples.

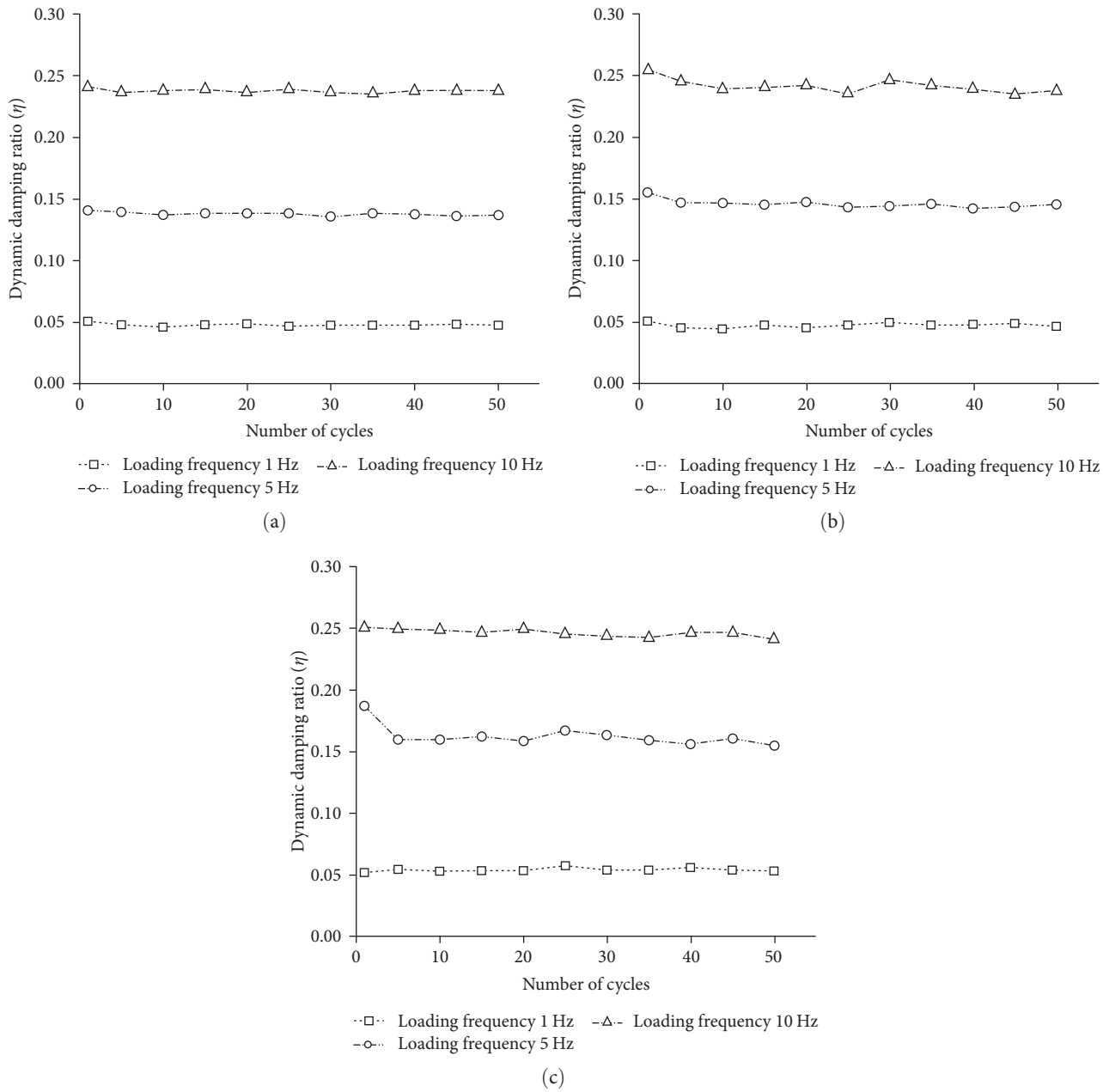

Figure 27: Dynamic damping ratio of samples with number of cycles and frequency: (a) single jointed 30° samples, (b) single jointed 60° samples, and (c) double jointed 30° samples.

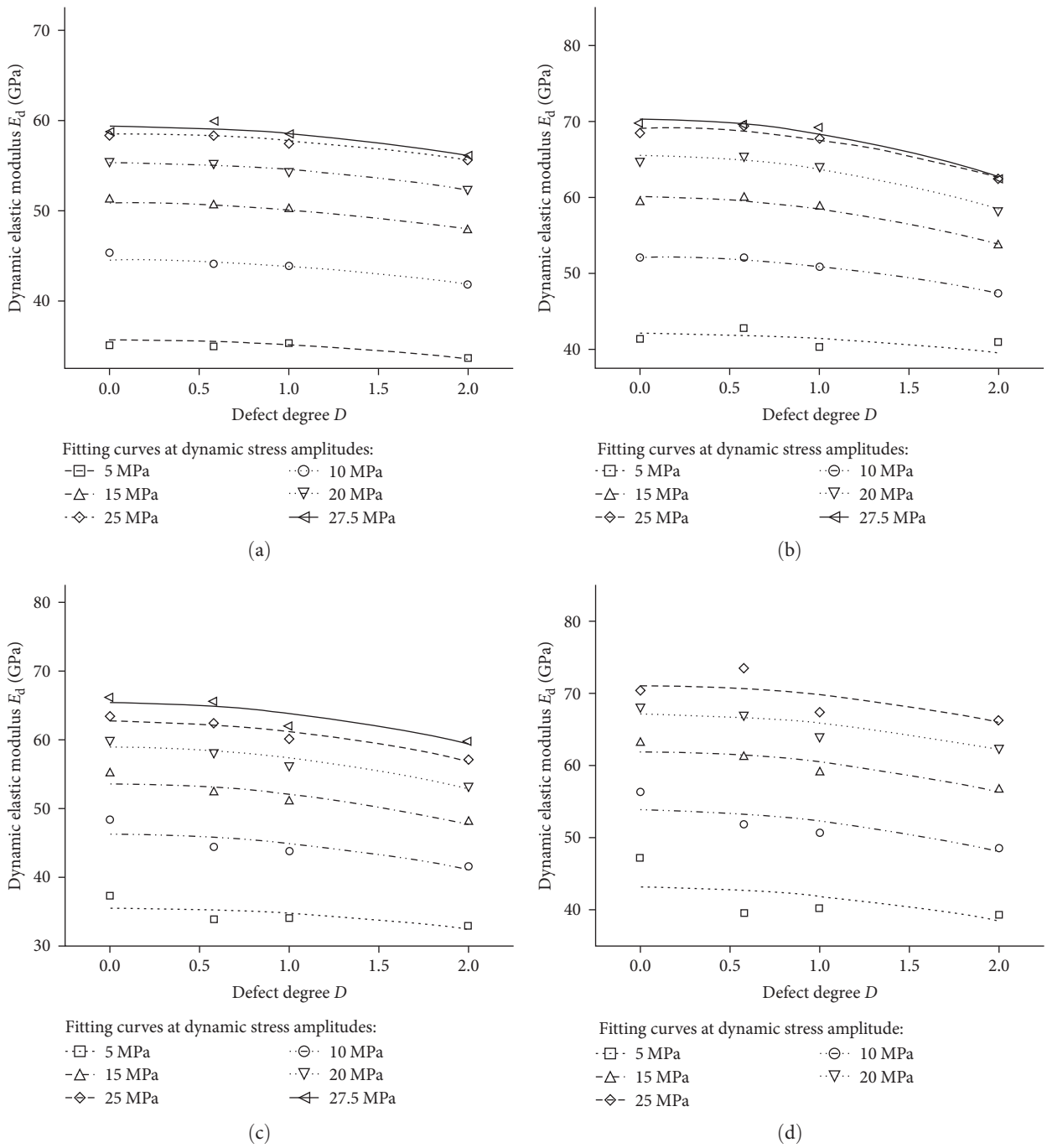

Figure 28: Dynamic elastic modulus of samples with defect degree: (a) 5 Hz and 5 MPa, (b) 5 Hz and 30 MPa, (c) 1 Hz and 20 MPa, and (d) 10 Hz and 20 MPa.

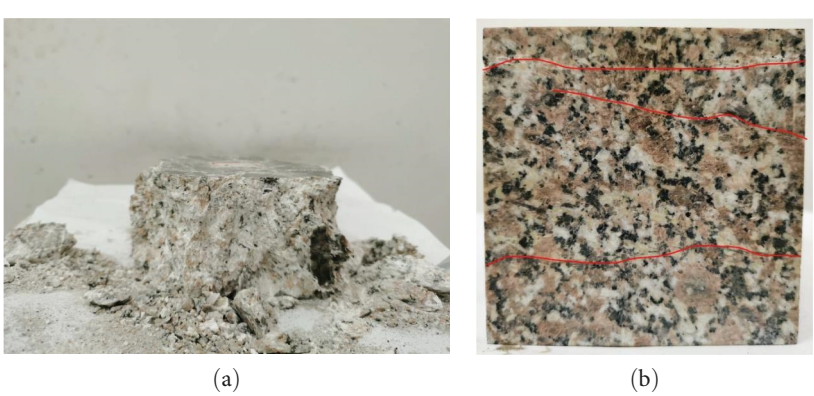

Figure 29: Sample loading comparison: (a) double jointed 30° sample and (b) intact sample.

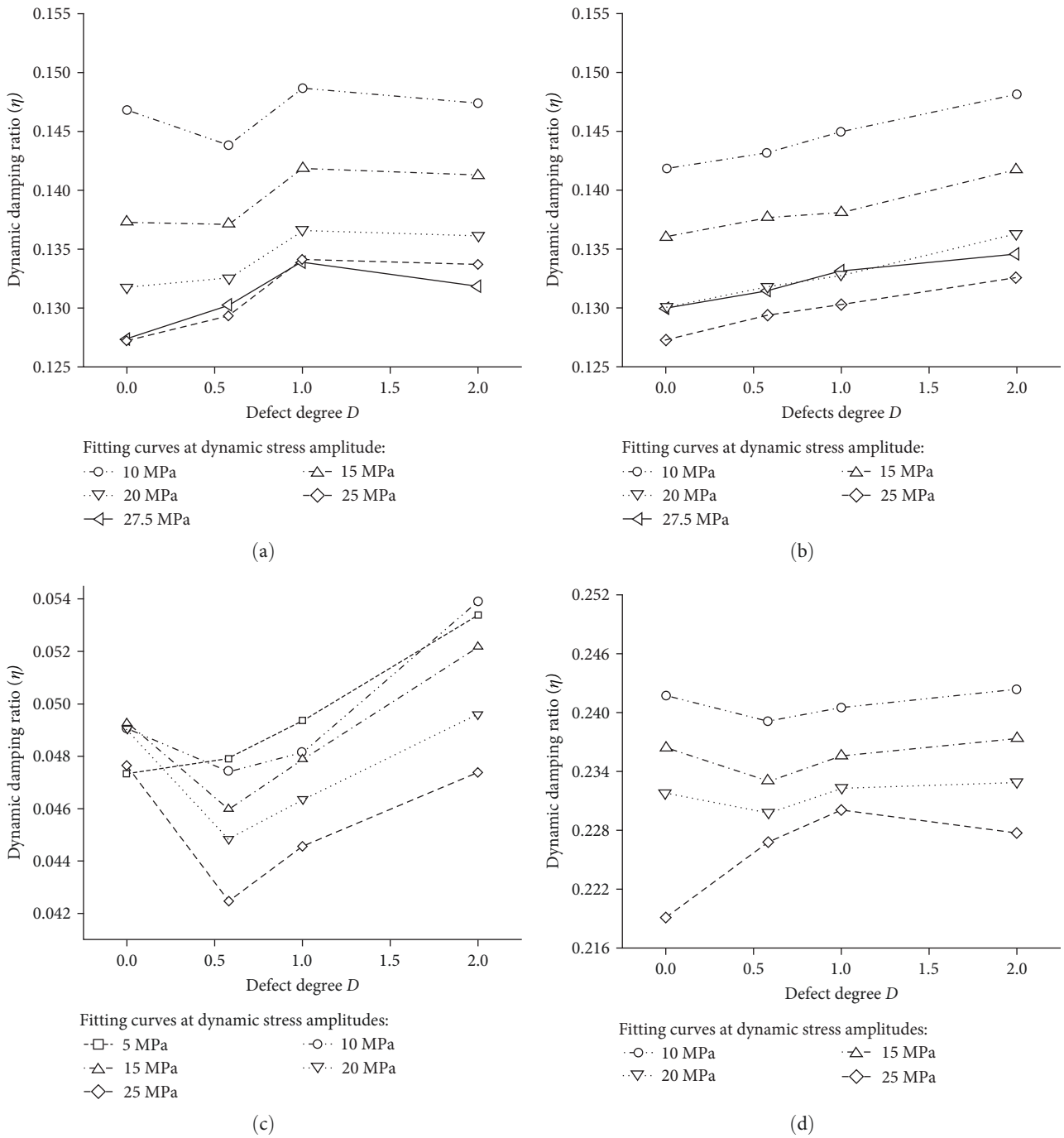

Figure 30: Dynamic damping ratio of samples with defect degree: (a) 5 Hz and 5 MPa, (b) 5 Hz and 30 MPa, (c) 1 Hz and 20 MPa, and (d) 10 Hz and 20 MPa.

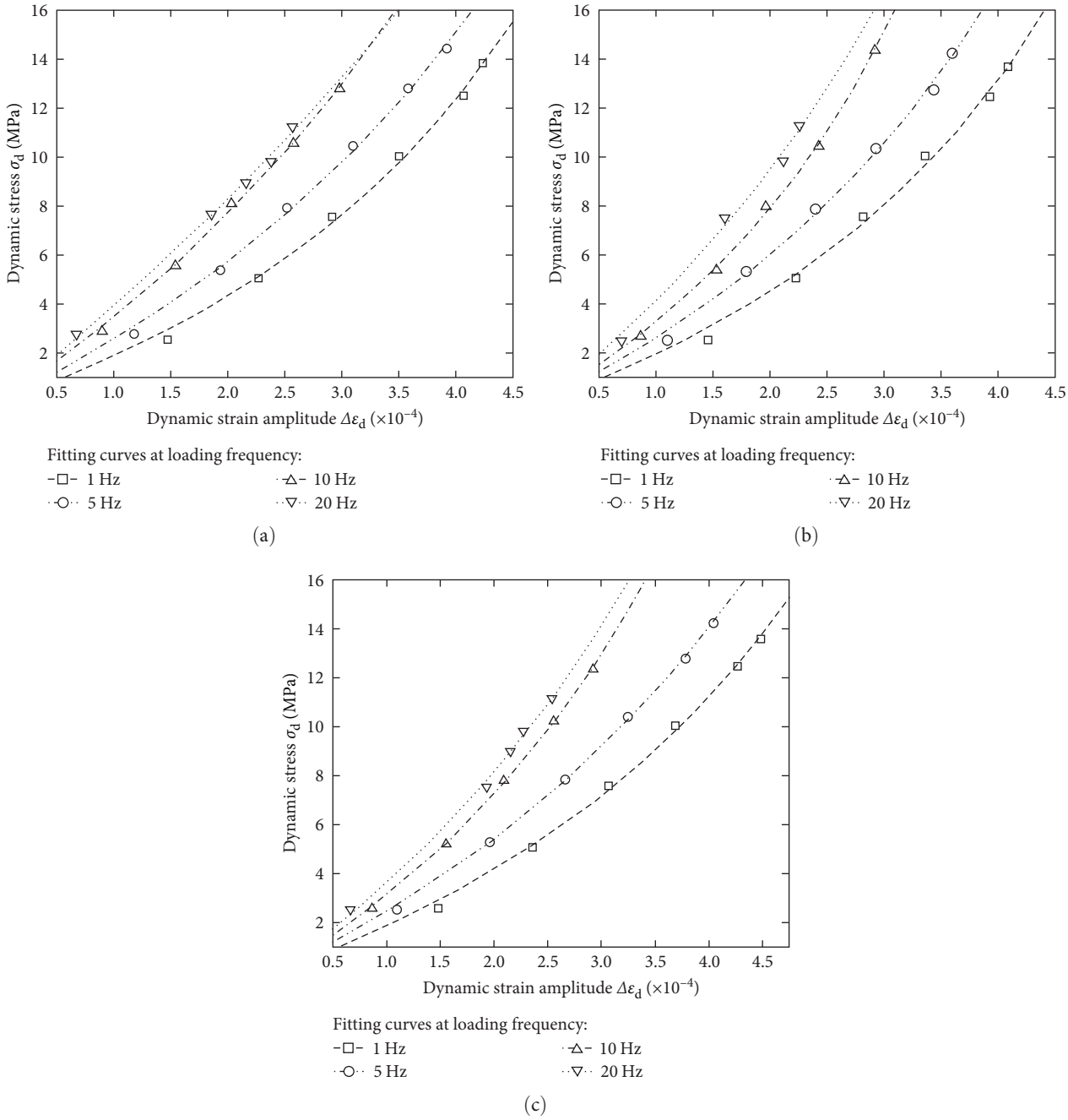

Figure 31: Sample fitting curves for Duncan–Chang model: (a) single jointed 30° samples, (b) single jointed 60° samples, and (c) double jointed 30° samples.

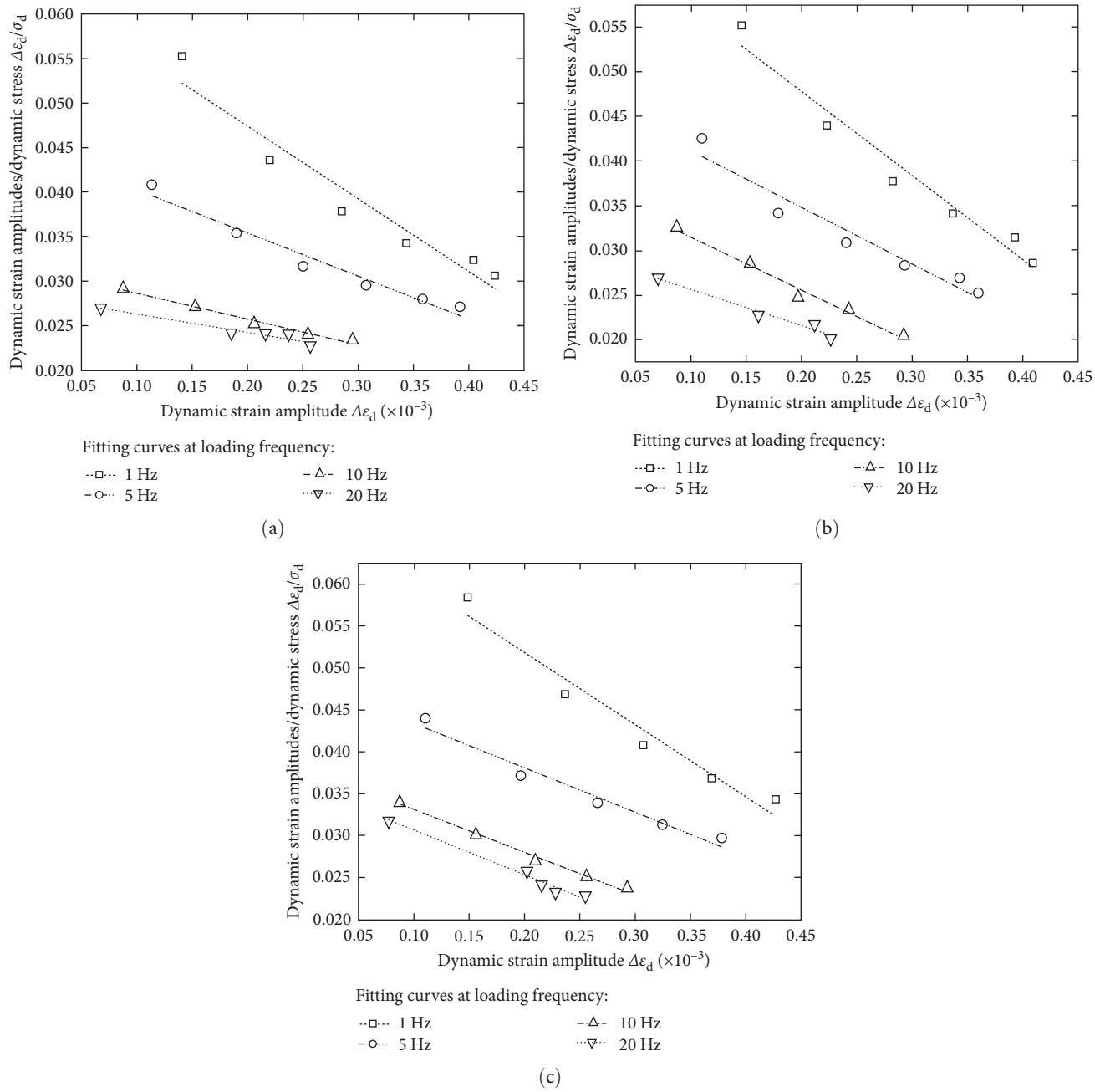

FIGURE 32: Samples' $\Delta\varepsilon_d/\sigma_d - \Delta\varepsilon_d$ fitting curves for Duncan–Chang model: (a) single jointed 30° samples, (b) single jointed 60° samples, and (c) double jointed 30° samples.

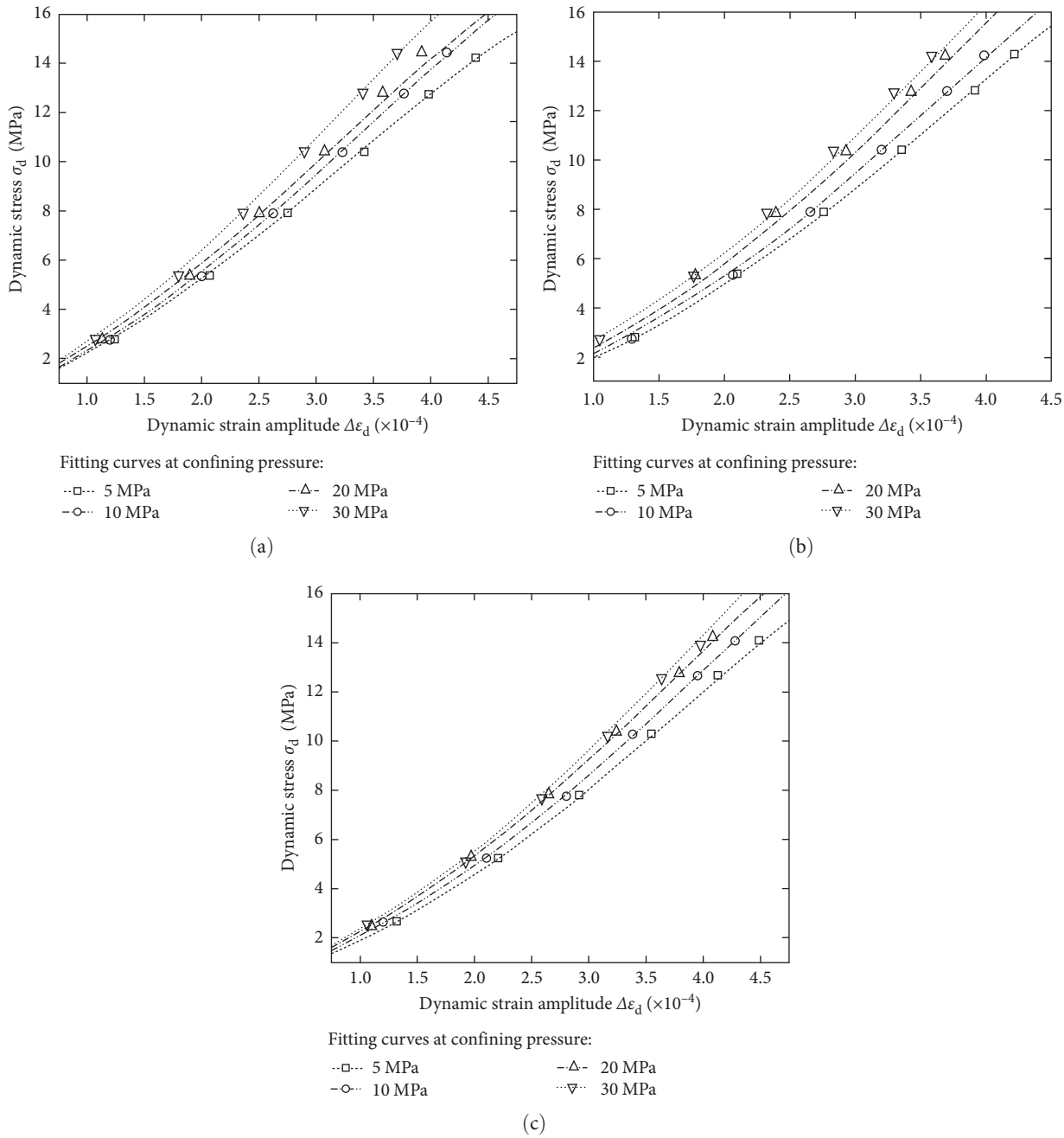

Figure 33: Sample fitting curves with confining pressure: (a) single jointed 30° samples, (b) single jointed 60° samples, and (c) double jointed 30° samples.

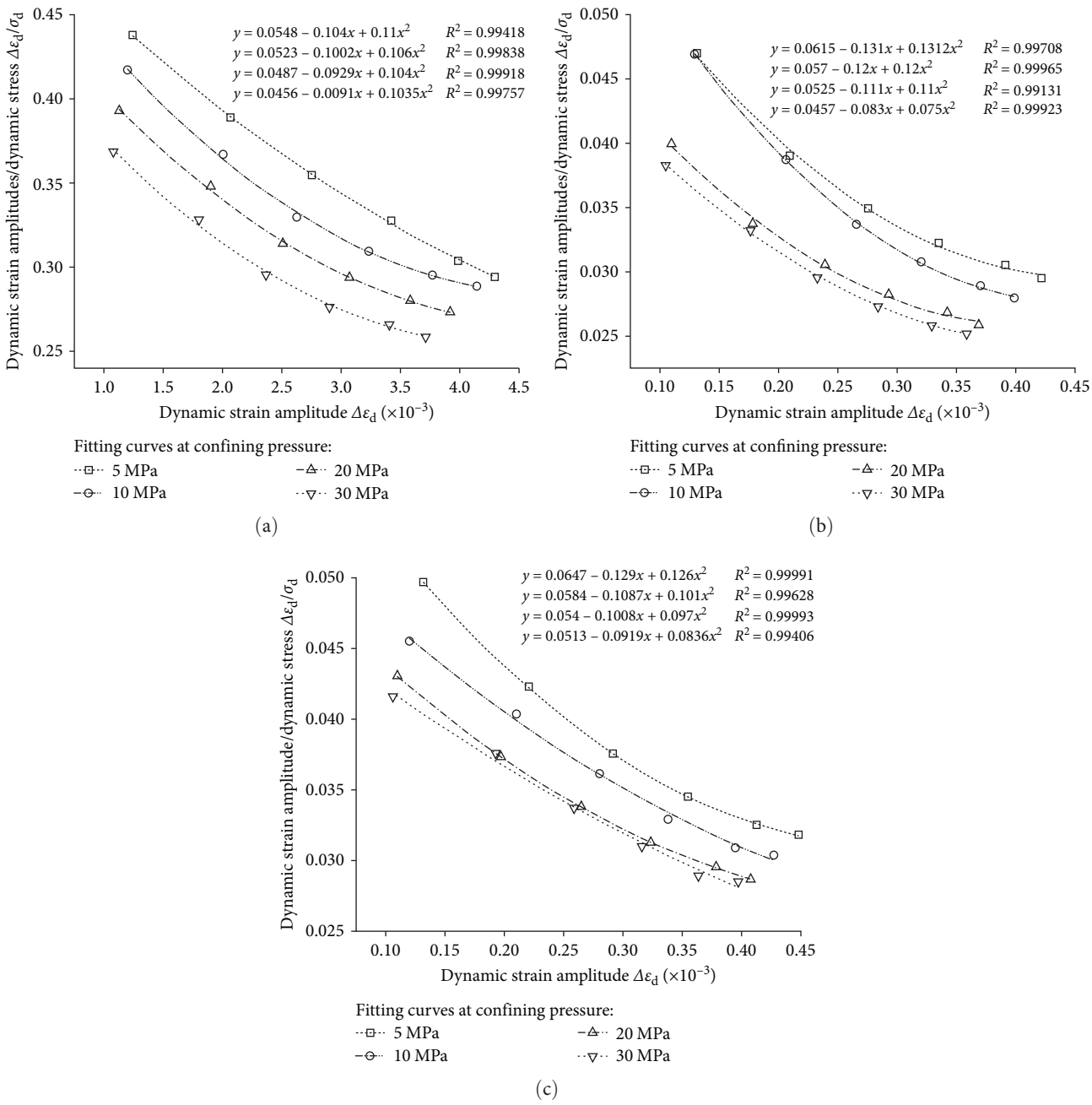

FIGURE 34: Samples' $\Delta\varepsilon_d/\sigma_d - \Delta\varepsilon_d$ fitting curves with confining pressure: (a) single jointed 30° samples, (b) single jointed 60° samples, and (c) double jointed 30° samples.

Table 5: The parameters a, b, and c change the curve with confining pressure.

Name	Parameter and confining pressure relationship equation
Single jointed 30° samples	$a = 0.0562 - 0.000363\sigma$ $b = -0.08931 + 0.00224 \times 0.9233$ $c = 0.1036 + 0.022 \times 0.78$
Single jointed 60° samples	$a = 0.064 - 0.000604\sigma$ $b = -0.1314 + 2.56 \times 10^{-4}\sigma + 4.3 \times 10^{-5}\sigma^2$ $c = 0.129 + 1.83 \times 10^{-4}\sigma - 6.55 \times 10^{-5}\sigma^2$
Double jointed 30° samples	$a = 0.0623 - 0.00502\sigma$ $b = -0.093 - 0.071 \times 0.087$ $c = 0.0873 + 0.0864 \times 0.85$

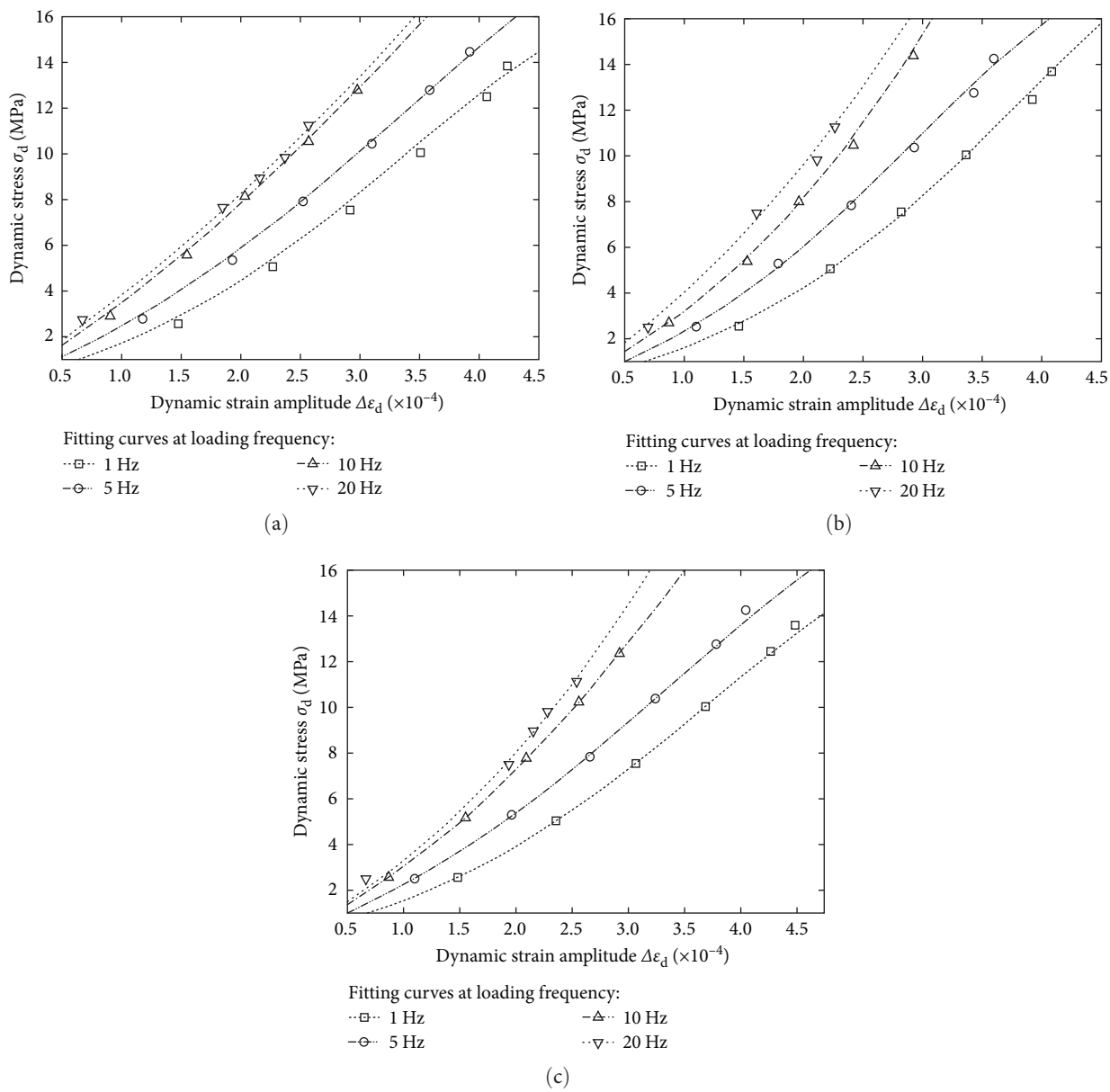

Figure 35: Sample fitting curves with frequency: (a) single jointed 30° samples, (b) single jointed 60° samples, and (c) double jointed 30° samples.

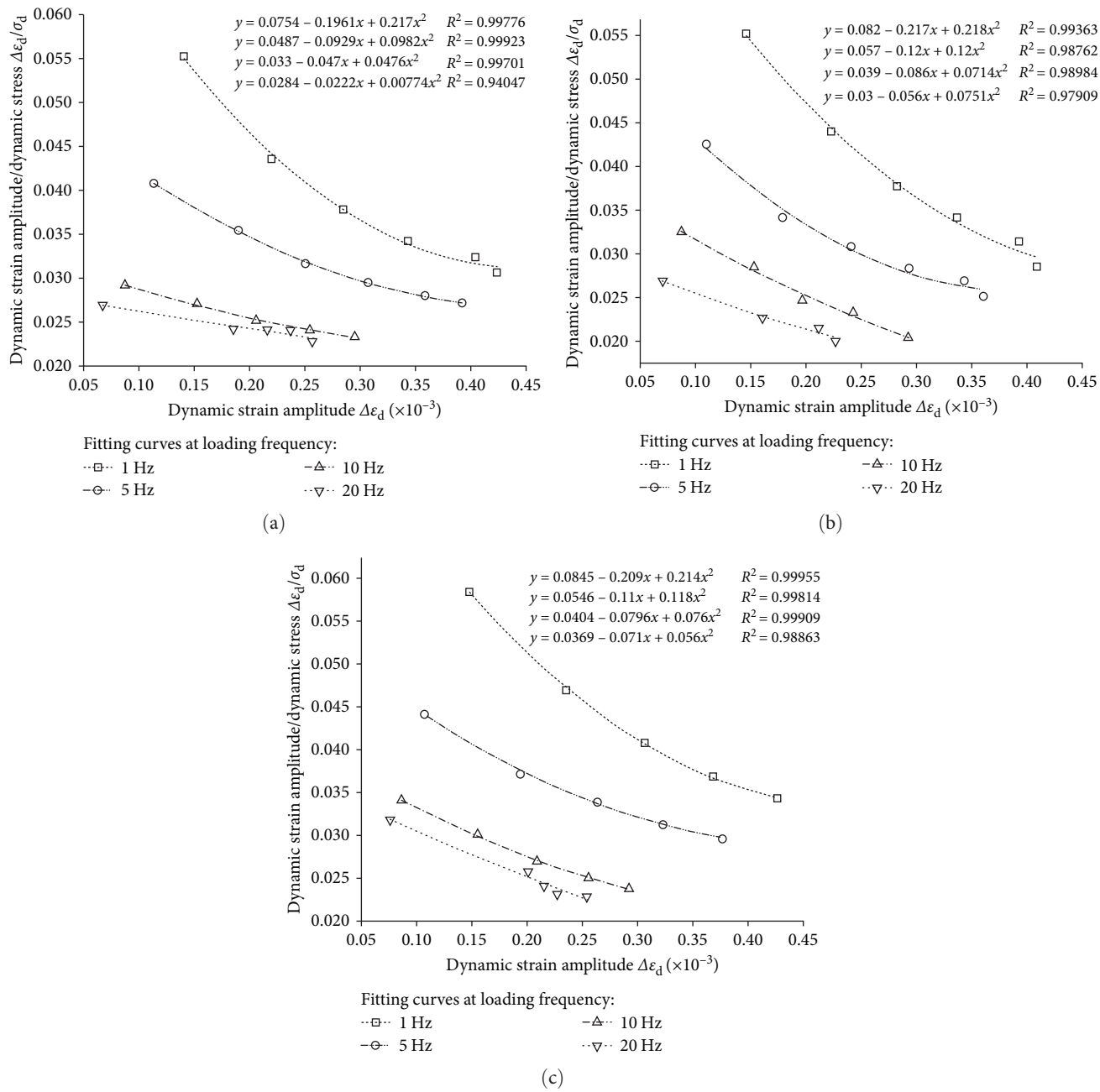

Figure 36: Samples' $\Delta\varepsilon_d/\sigma_d - \Delta\varepsilon_d$ fitting curves with frequency: (a) single jointed 30° samples, (b) single jointed 60° samples, and (c) double jointed 30° samples.

Table 6: The parameters a, b, and c change curve with frequency.

Name	Parameter versus frequency equation
Single jointed 30° samples	$a = 0.027 + 0.060 \times 0.81^f$ $b = -0.02 - 0.218 \times 0.81^f$ $c = 4.8 \times 10^{-3} + 0.0649 \times 0.842^f$
Single jointed 60° samples	$a = -0.027 + 0.0649 \times 0.89^f$ $b = -0.034 - 0.21 \times 0.89^f$ $c = -3.92 \times 10^{-3} + 0.26 \times 0.92^f$
Double jointed 30° samples	$a = 0.036 + 0.0623 \times 0.78^f$ $b = -0.071 - 0.189 \times 0.733^f$ $c = 0.054 + 0.2 \times 0.797^f$

influence on the dynamic properties of the sample compared to the confining pressure, which is consistent with the observations and conclusions presented in Chapters 3 and 4. The work we carry out in Part (II) will constantly modify the formulas of the parameters obtained from the experiments and finally derive the initial stress.

Table 6 shows the experimental parameters *a, b*, and *c* in relation to the variation of the frequency. It demonstrates that there is a power function relation between parameters *a, b, c* and loading frequency.

6. Conclusions

We controlled the confining pressure, loading frequency, dynamic stress amplitude, and number of cycles to perform triaxial tests on granite samples with different defect degrees, with the aim of constructing a back analysis model of the stress state of granite samples. We performed a study on the dynamic properties of granite samples in detail and used the data to construct a dynamic response model. The following conclusions are drawn:

(1) As the confining pressure increases, the dynamic elastic modulus of granite increases and its dynamic damping ratio decreases. From 5 to 10 MPa, the dynamic elastic modulus of single jointed 30° samples increased by a maximum of about 7.9%, the dynamic elastic modulus of single jointed 60° samples increased by a maximum of about 6.8%, and the dynamic elastic modulus of double jointed 30° samples increased by a maximum of about 10.9%. From 5 to 20 MPa, the dynamic elastic modulus of single jointed 30° samples increased by a maximum of about 12.8%, the dynamic elastic modulus of single jointed 60° samples increased by a maximum of about 20.5%, and the dynamic elastic modulus of double jointed 30° samples increased by a maximum of about 14.4%. From 5 to 30 MPa, the dynamic elastic modulus of single jointed 30° samples increased by a maximum of about 19.4%, the dynamic elastic modulus of single jointed 60° samples increased by a maximum of about 27.5%, and the dynamic elastic modulus of double jointed 30° samples increased by a maximum of about 24.0%. We hypothesize that this observed phenomenon can be attributed to the inhibition of microscopic crack propagation within the granite, leading to an increase in the dynamic elastic modulus. Additionally, the suppression of crack expansion reduces the energy generated during loading, consequently resulting in a gradual decrease in the dynamic damping ratio of the granite. However, the trend of decreasing dynamic damping ratio of granite is not obvious in single jointed 60° and double jointed 30° granite. We believe that this is related to the fact that insufficient close contact occurred between the granite interiors after the granites were cut, and increasing the confining pressure in a short time could not reduce the dynamic damping ratio.

(2) The dynamic elastic modulus and dynamic damping ratio of the sample increase with increasing frequency. From 1 to 5 Hz, the dynamic elastic modulus of single jointed 30° samples increased by a maximum of about 15.4%, the dynamic elastic modulus of single jointed 60° samples increased by a maximum of about 20.4%, and the dynamic elastic modulus of double jointed 30° samples increased by a maximum of about 14.4%. From 1 to 10 Hz, the dynamic elastic modulus of single jointed 30° samples increased by a maximum of about 21.7%, the dynamic elastic modulus of single jointed 60° samples increased by a maximum of about 20.4%, and the dynamic elastic modulus of double jointed 30° samples increased by a maximum of about 23.4%. From 1 to 20 Hz, the dynamic elastic modulus of single jointed 30° samples increased by a maximum of about 74.1%, the dynamic elastic modulus of single jointed 60° samples increased by a maximum of about 80.6%, and the dynamic elastic modulus of double jointed 30° samples increased by a maximum of about 80.3%. The dynamic properties of granite are greatly affected at a frequency of 20 Hz, comparing to confining pressure. We suspect that it is due to the wedging of granite internal particles fell into the cracks inside the rock and caused them to close, causing the granite strength increased significantly. And the viscous resistance of the fluid between the mineral particles was

enhanced, and more energy was consumed when the mineral particles produce displacement, then the dynamic damping ratio also gradually increased.

(3) The dynamic elastic modulus of granite increases with the increasing dynamic stress amplitude, but its dynamic damping ratio decreases. We believe that it is caused by the large dynamic stress amplitude compacting the internal defects and mineral grains of the granite. The data of the dynamic damping ratio of granite are more discrete in the fitting curve, and we think that the effect of dynamic stress amplitude on the growth of the dynamic damping ratio of granite is smaller compared with the confining pressure and frequency.

(4) The dynamic elastic modulus and dynamic damping ratio of granite decreases with an increasing number of cycles. As the number of cycles increased, the irreversible deformation of the nodular rock samples subjected to cyclic loading was gradually developed, causing the dynamic elastic modulus of granite decreased. At the same time, the irreversible deformation generated at the beginning of the cycle, the higher energy dissipation required to store the lower level of elastic energy. Leading to a higher dynamic damping ratio of granite at the beginning of the cycles and then decreasing.

(5) We defined a defect degree D to display the variation dynamic elastic modulus and dynamic damping ratio of the sample with increasing defect degree. As the defect degree of granite increases, the dynamic elastic modulus decreases, but its dynamic damping ratio increases. We believe that this is related to the transverse cracks produced during loading and the pores created inside the granite after cutting.

(6) We improved the Duncan–Chang model to obtain the dynamic stress–strain relationship for the granite sample at different pressure, loading amplitude, and frequencies. The model fits the data well, with most formulas reaching a correlation coefficient of 0.98. However, the frequency has a large effect on the material performance parameters, comparing the confining pressure. The lowest granite dynamic response model was only 0.94 at a frequency of 20 Hz. The data obtained from this experiment and the constructed dynamic response model will be applied to our study in Part (II).

Data Availability

The data used to support the findings of this study are included within the article.

Conflicts of Interest

On behalf of all authors, the corresponding author states that there is no conflict of interest.

Acknowledgments

This research was financially supported by the National Natural Science Foundation of China (grant no. 41827807) and the Guangdong Provincial Key Laboratory of Modern Civil Engineering Technology (2021B1212040003). All the sources of support are gratefully acknowledged.

References

[1] H. Aghaei, G. M. Penkov, D. A. Solomoichenko et al., "Density-dependent relationship between changes in ultrasonic wave velocities, effective stress, and petrophysical-elastic properties of sandstone," *Ultrasonics*, vol. 132, Article ID 106985, 2023.

[2] J. F. Jin, Y. C. Zhang, K. Liu, R. Zhang, and Y. H. Li, "Effect of gradient stress on stress wave propagation characteristics of red sandstone," *Rock and Soil Mechanics*, vol. 44, pp. 952–964, 2023.

[3] P. Jia, P. Zhu, B. Li, and X. Xu, "Characteristics of real-time ultrasonic wave during uniaxial compression of rock," *Journal of Central South University*, vol. 53, pp. 3967–3977, 2022.

[4] Y. Cheng, Z. Song, X. Chang, and T. Yang, "Investigating the frequency spectrum characteristic of stress wave under multistage loading stress," *Advances in Civil Engineering*, vol. 2022, Article ID 7761639, 13 pages, 2022.

[5] X. B. Li, T. S. Lok, and J. Zhao, "Dynamic characteristics of granite subjected to intermediate loading rate," *Rock Mechanics and Rock Engineering*, vol. 38, no. 1, pp. 21–39, 2005.

[6] M. N. Bagde and V. Petroš, "Fatigue properties of intact sandstone samples subjected to dynamic uniaxial cyclical loading," *International Journal of Rock Mechanics and Mining Sciences*, vol. 42, no. 2, pp. 237–250, 2005.

[7] L.-J. Ma, X.-Y. Liu, M.-Y. Wang et al., "Experimental investigation of the mechanical properties of rock salt under triaxial cyclic loading," *International Journal of Rock Mechanics and Mining Sciences*, vol. 62, pp. 34–41, 2013.

[8] N. Li, W. Chen, P. Zhang, and G. Swoboda, "The mechanical properties and a fatigue-damage model for jointed rock masses subjected to dynamic cyclical loading," *International Journal of Rock Mechanics and Mining Sciences*, vol. 38, no. 7, pp. 1071–1079, 2001.

[9] Y. Liu, F. Dai, P. Fan, N. Xu, and L. Dong, "Experimental investigation of the influence of joint geometric configurations on the mechanical properties of intermittent jointed rock models under cyclic uniaxial compression," *Rock Mechanics and Rock Engineering*, vol. 50, no. 6, pp. 1453–1471, 2017.

[10] Q. Lin, P. Cao, S. Mao, C. Ou, and R. Cao, "Fatigue behaviour and constitutive model of yellow sandstone containing pre-existing surface crack under uniaxial cyclic loading," *Theoretical and Applied Fracture Mechanics*, vol. 109, Article ID 102776, 2020.

[11] H. F. Deng, Y. Hu, J. L. Li, Z. Wang, X. J. Zhang, and H. B. Zhang, "Effects of frequency and amplitude of cyclic loading on the dynamic characteristics of sandstone," *Rock and Soil Mechanics*, vol. 12, pp. 3402–3409, 2017.

[12] X. H. Ni, "Failure characteristic of granite under cyclic loading with different frequencies," *Applied Mechanics and Materials*, vol. 638–640, pp. 1967–1970, 2014.

[13] C.-X. Huang, X.-H. Wang, H. Zhou, and D.-C. Qin, "Dynamic elastic modulus and damping ratio of unsaturated red clay,"

Geotechnical and Geological Engineering, vol. 38, no. 1, pp. 873–881, 2020.

[14] P. F. Bie and H. X. Liu, "Influence of stress amplitude on the dynamic characteristics of phyllite samples under triaxial multi-stage cyclic loading," in *China Rock*, vol. 570 of *IOP Conference Series: Earth and Environmental Science*, pp. 23–26, IOP Publishing Ltd, Beijing, China, October,2020.

[15] S.-Q. Yang, Y. Li, G.-W. Ma et al., "Experiment and numerical simulation study of dynamic mechanical behavior of granite specimen after high temperature treatment," *Computers and Geotechnics*, vol. 154, Article ID 105111, 2023.

[16] Y. Zhao, S. Dang, J. Bi, C. Wang, F. Gan, and J. Li, "Energy evolution characteristics of sandstones during confining pressure cyclic unloading conditions," *Rock Mechanics and Rock Engineering*, vol. 56, no. 2, pp. 953–972, 2023.

[17] X. Xie, J. Li, and Y. Zheng, "Experimental study on dynamic mechanical and failure behavior of a jointed rock mass," *International Journal of Rock Mechanics and Mining Sciences*, vol. 168, Article ID 105415, 2023.

[18] J. Xiao, X. Feng, D. Ding, and F. Jiang, "Study of hysteresis and damping effects of rock subjected to constant amplitude cyclic loading," *Chinese Journal of Rock Mechanics and Engineering*, vol. 29, pp. 1677–1683, 2010.

[19] J. Xu, Y. Kang, Z. Wang, X. Wang, D. Zeng, and D. Su, "Dynamic mechanical behavior of granite under the effects of strain rate and temperature," *International Journal of Geomechanics*, vol. 20, no. 2, Article ID 04019177, 2019.

[20] P. Xiao, D.-Y. Li, G.-Y. Zhao, Q.-Q. Zhu, H.-X. Liu, and C.-S. Zhang, "Mechanical properties and failure behavior of rock with different flaw inclinations under coupled static and dynamic loads," *Journal of Central South University*, vol. 27, no. 10, pp. 2945–2958, 2020.

[21] W. Yin, Z. Feng, and Y. Zhao, "Effect of grain size on the mechanical behaviour of granite under high temperature and triaxial stresses," *Rock Mechanics and Rock Engineering*, vol. 54, no. 2, pp. 745–758, 2021.

[22] G. Zhao, Y. Hu, and P. Jin, "Exploratory experimental study on the mechanical properties of granite subjected to cyclic temperature and uniaxial stress," *Energies*, vol. 13, no. 8, Article ID 2061, 2020.

[23] Y.-H. Huang, S.-Q. Yang, and Y.-S. Bu, "Effect of thermal shock on the strength and fracture behavior of pre-flawed granite specimens under uniaxial compression," *Theoretical and Applied Fracture Mechanics*, vol. 106, Article ID 102474, 2020.

[24] J. Zhao and T. Zhang, "Experimental study on mechanical properties of deep buried granite under different confining pressures," *Advances in Civil Engineering*, vol. 2020, Article ID 6640497, 10 pages, 2020.

[25] X.-P. Zhou, G.-Q. Li, and H.-C. Ma, "Real-time experiment investigations on the coupled thermomechanical and cracking behaviors in granite containing three pre-existing fissures," *Engineering Fracture Mechanics*, vol. 224, Article ID 106797, 2020.

[26] S. F. Wu, Q. C. Zhang, S. L. Li, B. Chen, and D. S. Liu, "Impact mechanical characteristics and damage evolution model of granite," *Meitan Xuebao/Journal of the China Coal Society*, vol. 41, pp. 2756–2763, 2016.

[27] T.-B. Yin, R.-H. Shu, X.-B. Li, P. Wang, and L.-J. Dong, "Combined effects of temperature and axial pressure on dynamic mechanical properties of granite," *Transactions of Nonferrous Metals Society of China*, vol. 26, no. 8, pp. 2209–2219, 2016.

[28] P. Li, M. Cai, Y. Gao et al., "Mechanical responses and fracturing behavior of jointed rock masses with a cavity under different dynamic loads," *International Journal of Impact Engineering*, vol. 178, Article ID 104608, 2023.

[29] S. Liang, T. Ling, D. Liu, and S. Li, "On dynamic constitutive model of granite under impact loading: effect of damage on dynamic strength," in *5th International Conference on Environmental Science and Civil Engineering (ESCE2019)*, vol. 283 of *IOP Conference Series: Earth and Environmental Science*, pp. 13-14, IOP Publishing Ltd, Nanchang, China, April, 2019.

[30] S. Mishra, T. Chakraborty, V. Matsagar, J. Loukus, and B. Bekkala, "High strain-rate characterization of Deccan trap rocks using SHPB device," *Journal of Materials in Civil Engineering*, vol. 30, no. 5, Article ID 04018059, 2018.

[31] H. Guo, W. Guo, Y. Zhai, and Y. Su, "Experimental and modeling investigation on the dynamic response of granite after high-temperature treatment under different pressures," *Construction and Building Materials*, vol. 155, pp. 427–440, 2017.

[32] D. Li, C. Hu, and Q. Zhu, "Experimental study on mechanical properties and failure laws of granite with an artificial flaw under coupled static and dynamic loads," *Chinese Journal of Rock Mechanics and Engineering*, vol. 39, pp. 1081–1093, 2020.

[33] B. Yang, M. He, Z. Zhang, J. Zhu, and Y. Chen, "Experimental investigation and empirical model on damping properties of rock under multistage cyclic loading," *Soil Dynamics and Earthquake Engineering*, vol. 163, Article ID 107557, 2022.

[34] X. Ding, J. Zhao, Y. Dong, and M. Zhou, "A thorough investigation of the dynamic properties of granite under cyclic loading," *Applied Sciences*, vol. 13, no. 22, Article ID 12514, 2023.

[35] Y. Liu, F. Dai, L. Dong, N. Xu, and P. Feng, "Experimental investigation on the fatigue mechanical properties of intermittently jointed rock models under cyclic uniaxial compression with different loading parameters," *Rock Mechanics and Rock Engineering*, vol. 51, no. 1, pp. 47–68, 2018.

[36] B. J. Brennan and F. D. Stacey, "Frequency dependence of elasticity of rock—test of seismic velocity dispersion," *Nature*, vol. 268, pp. 220–222, 1977.

[37] H. Zhang, M. Chen, X. Meng, N. Mu, and H. Liu, "Damage model and mechanical characteristics of jointed rock mass with different joint dip angles," *Journal of Harbin Engineering University*, vol. 43, pp. 801–808, 2022.

[38] M. Chen, C.-W. Zang, Z.-W. Ding et al., "Effects of confining pressure on deformation failure behavior of jointed rock," *Journal of Central South University*, vol. 29, pp. 1305–1319, 2022.

[39] F. Zhao, L. Chang, and W. Zhang, "Experimental investigation of dynamic shear modulus and damping ratio of Qinghai-Tibet frozen silt under multi-stage cyclic loading," *Cold Regions Science and Technology*, vol. 170, Article ID 102938, 2020.

[40] W. H. Peellage, B. Fatahi, and H. Rasekh, "Experimental investigation for vibration characteristics of jointed rocks using cyclic triaxial tests," *Soil Dynamics and Earthquake Engineering*, vol. 160, Article ID 107377, 2022.

[41] L. Qian, T. Yao, Z. Mo et al., "Experimental study on crack evolution behavior and constitutive model of granite based on the deviatoric stress to peak strength ratio," *Bulletin of Engineering Geology and the Environment*, vol. 81, no. 7, 2022.

[42] D. Xi, Y. Chen, Y. Tao, and Y. Liu, "Nonlinear elastic hysteric characteristics of rocks," *Yanshilixue Yu Gongcheng Xuebao/*

Chinese Journal of Rock Mechanics and Engineering, vol. 25, pp. 1086–1093, 2006.

[43] D. Xi, X. Liu, and C. Zhang, "Analysis on micro and meso-damage of rock by macro-hysteresis curve," *Chinese Journal of Rock Mechanics and Engineering*, vol. 22, no. 2, pp. 182–187, 2003.

[44] K. Peng, J. Zhou, Q. Zou, and X. Song, "Effect of loading frequency on the deformation behaviours of sandstones subjected to cyclic loads and its underlying mechanism," *International Journal of Fatigue*, vol. 131, Article ID 105349, 2020.

[45] M. Nie, J. Xu, H. Ren, and J. Liu, "Dynamic triaxial experimental research on damping parameters and dynamic elastic parameters for marble," *Chinese Journal of Rock Mechanics and Engineering*, vol. 30, no. Supp. 2, pp. 3989–3994, 2011.

[46] J. Liu, H. Xie, J. Xu, and J. Pei, "Discussion on deformation and damping parameters of rock under cyclic loading," *Chinese Journal of Rock Mechanics and Engineering*, vol. 31, no. 4, pp. 770–777, 2012.

[47] M. M. He, Z. Q. Zhang, and N. Li, "Experimental investigation and empirical model to determine the damping and shear stiffness properties of soft rock under multistage cyclic loading," *Soil Dynamics and Earthquake Engineering*, vol. 147, Article ID 106818, 2021.

[48] Z. Wang, S. Li, L. Qiao, and J. Zhao, "Fatigue behavior of granite subjected to cyclic loading under triaxial compression condition," *Rock Mechanics and Rock Engineering*, vol. 46, no. 6, pp. 1603–1615, 2013.

[49] Y. Wang, Y. Z. Hu, and S. H. Gao, "Dynamic mechanical behaviors of interbedded marble subjected to multi-level uniaxial compressive cyclic loading conditions: an insight into fracture evolution analysis," *Engineering Fracture Mechanics*, vol. 241, Article ID 107410, 2021.

[50] J. M. Duncan and C.-Y. Chang, "Nonlinear analysis of stress and strain in soils," *Journal of the Soil Mechanics and Foundations Division*, vol. 96, no. 5, pp. 1629–1653, 1970.

[51] H. Zhu, X. Tang, F. Zhang, and J. D. McLennan, "Mechanical behavior of methane-hydrate–bearing sand with nonlinear constitutive model," *Arabian Journal for Science and Engineering*, vol. 47, no. 9, pp. 12141–12167, 2022.

[52] L. Ma and X. Xu, "Mechanical behavior and constitutive model of methane hydrate bearing sediments," *Geomechanics and Geophysics for Geo-Energy and Geo-Resources*, vol. 7, no. 3, 2021.

[53] M. Yan, R. Yan, and H. Yu, "Strain-softening characteristics of hydrate-bearing sediments and modified Duncan–Chang model," *Advances in Materials Science and Engineering*, vol. 2021, Article ID 2809370, 15 pages, 2021.